REPORT DOCUMENTATION PAGE
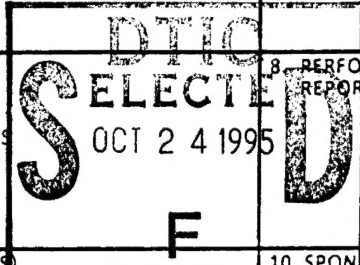
Public reporting burden for this collection of information is estimated to average 1 hour per response, including the time for reviewing instructions, searching existing data sources, gathering and maintaining the data needed, and completing and reviewing the collection of information. Send comments regarding this burden estimate or any other aspect of this collection of information, including suggestions for reducing this burden, to Washington Headquarters Services, Directorate for Information Operations and Reports, 1215 Jefferson Davis Highway, Suite 1204, Arlington, VA 22202-4302, and to the Office of Management and Budget, Paperwork Reduction Project (0704-0188), Washington, DC 20503.

1. AGENCY USE ONLY (Leave blank)	2. REPORT DATE August 4, 1995	3. REPORT TYPE AND DATES COVERED Final Report, 5/1/92 - 5/31/95

4. TITLE AND SUBTITLE

The Interaction of UV-Laser Radiation with Metal and Semiconductor Surfaces

5. FUNDING NUMBERS

DAAL03-92-G-0191

6. AUTHOR(S)

Prof. Richard M. Osgood, Jr.

7. PERFORMING ORGANIZATION NAME(S) AND ADDRESS(ES)

Columbia University
Microelectronics Sciences Laboratories
1001 Schapiro CEPSR
New York, NY 10027

DTIC
SELECTED
OCT 24 1995
F

8. PERFORMING ORGANIZATION REPORT NUMBER

9. SPONSORING/MONITORING AGENCY NAME(S) AND ADDRESS(ES)

U.S. Army Research Office
P. O. Box 12211
Research Triangle Park, NC 27709-2211

10. SPONSORING/MONITORING AGENCY REPORT NUMBER

ARO 29391.2-PH

11. SUPPLEMENTARY NOTES

The view, opinions and/or findings contained in this report are those of the author(s) and should not be construed as an official Department of the Army position, policy, or decision, unless so designated by other documentation.

12a. DISTRIBUTION/AVAILABILITY STATEMENT

Approved for public release; distribution unlimited.

12b. DISTRIBUTION CODE

1951023 035

13. ABSTRACT (Maximum 200 words)

This report describes significant progress in nonlinear-photoemission studies of electron localization and scattering processes in low-dimensional electron systems. We have improved considerably a previously developed two-photon photoemission technique, and we have made the first momentum- and energy-resolved measurements of two-dimensional electron scattering and localization in alkali-noble metal interfaces as well as one-dimensional electron localization and confinement effects on stepped single-crystal surfaces of monatomic step height and nanometer step spacings. In particular, we extended our measurements of image states to image-potential resonances on single-crystal metal systems. By utilizing the unique energy-band structure of $Cu(111)$, we investigated the relaxation dynamics of image-state electrons. We successfully distinguished elastic and inelastic scattering processes for two-dimensional excited-state electrons and obtained empirical scattering cross-sections, which are found to be proportional to the electron momentum parallel to the surface. Our work in image-state spectroscopy also initiated a collaboration with an IBM research group. This collaboration has resulted in the observation of lateral superlattice effects and disorder localization effects on vicinal copper surfaces, providing new insights to the physics of nanostructures.

14. SUBJECT TERMS

Metal-alkyls, photodeposition, laser photoemission, UV lasers, Two-photon photoemission, single crystal Cu, excimer laser

15. NUMBER OF PAGES

60

16. PRICE CODE

17. SECURITY CLASSIFICATION OF REPORT UNCLASSIFIED	18. SECURITY CLASSIFICATION OF THIS PAGE UNCLASSIFIED	19. SECURITY CLASSIFICATION OF ABSTRACT UNCLASSIFIED	20. LIMITATION OF ABSTRACT UL

THE INTERACTION OF ULTRAVIOLET LASER RADIATION
WITH METAL AND SEMICONDUCTOR SURFACES

FINAL REPORT

Richard M. Osgood, Jr.
Principal Investigator

May 1, 1992 through May 31, 1995

U. S. Army Research Office

CONTRACT # DAAL-03-92-G-0191

Columbia Radiation Laboratory
Columbia University
New York, New York 10027

APPROVED FOR PUBLIC RELEASE
DISTRIBUTION UNLIMITED

Submitted August 4, 1995

1

TABLE OF CONTENTS

Introduction: Image-State Spectroscopic Studies of Electronic Structures and Scattering Processes in Low-Dimensional (1D and 2D) Systems

The first observations of image states on solid surfaces were reported about ten years ago using inverse photoemission[1] and two-photon photoemission (2PPE),[2] and the initial stages in the nonlinear spectroscopy of image states emphasized the measurement of the binding energies of these states as well as their dispersion relations or effective masses.[3] More recently, work in this area has sought to exploit the relative precision of image-state spectroscopy by using their high-resolution two-photon photoemission spectra as a probe of surface conditions as well as the interfacial physics.[4-11] Simultaneously with this work, the image-state spectroscopy has been developed into a powerful and unique probe of surface/near-surface electronic structures and electron dynamics, enabling new insights into the physics of nanostructured.[12,13] ARO support of this program has enabled us to make significant progress in uncovering the physics of low-dimensional electron systems, utilizing the high-resolution angle-resolved 2PPE. Our progress is reported below in four sections.

I. Image-Potential Resonances

Two-photon photoemission spectroscopy (2PPE) is a suitable technique for probing unoccupied bound states at crystal surfaces. Typically, it utilizes a real intermediate state, with the first photon populating an excited state, while the second photoemits from this level. This spectroscopy has been used with a great deal of success in studying image-potential (IP) states in metals, through the determination of their binding energies, lifetimes and effective masses. The

2PPE spectroscopy of these states is relatively easily realized because of their relatively long lifetimes, *i.e.* 10^{-12}s, compared to those of bulk states, 10^{-14}–10^{-15}s. Given the advantages of 2PPE, it would be of much interest if the technique could also be applied to shorter-lifetime, bulk-like states without resorting to femtosecond pulses which have been used, for example, to examine short lived surface states on semiconductor surfaces.[14]

In this section, we report that two-photon spectroscopy with a tunable nanosecond source can be applied to measure short-lived surface resonance states on metal surfaces. In particular, we have measured the photoemission spectra from surface resonances resulting from strong mixing of an image state with a bulk energy band. These strong image resonances have recently become of interest since they provide a clear example of a well defined, calculable surface resonance system. In particular, in contrast to an image state which is formed by an electron reflecting between the Coulombic and the crystal barrier, an image resonance is formed by reflection between the same surface Coulombic barrier and an inner discontinuity in the surface potential. Quantum mechanically we would expect an increased broadening of the image feature as the degree of coupling to the bulk is increased, a phenomena which has been discussed in conjunction with the dependence on the principal quantum number of image states[15-17] and the analogous broadening of discrete energy levels of an adsorbed atom on a metal surface.[18-20] While several papers have investigated these resonances theoretically, there have been only a very limited set of corresponding experimental measurements. Typically these have relied on inverse photoemission and, thus, have had generally low resolution.

A. On Copper Surfaces

Two-photon spectroscopy was first used to measure image states on the (111) faces of

Cu[21,22] and Ag[23,24] for which the n=1 image state is close to degenerate with bulk bands. Here a narrow surface state that lay below E_F in the band gap of the projected band structure was used as the initial source of electrons in the 2PPE process (Fig. 1).
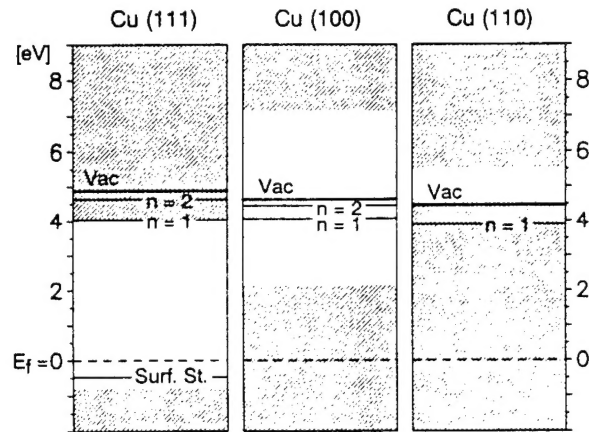
Figure 1. Projected energy-band diagrams for Cu(111),[22] Cu(100),[25] and Cu(110)[45,47] at $k_{\parallel} = 0$. The shaded area represents the projection of the bulk band structure. Image states are designated by "n = 1" and "n = 2".

Because of this narrow initial state, the 2PPE signal would be expected to be particularly strong since the density of states for the narrow surface state is much higher than that of the bulk continuum initial levels, which are important in the cases of Cu(110) and Cu(100). Also, the transition matrix element is bigger for the overlap of surface state wave function than for the overlap of the bulk wave function with the image state.[24,25] Subsequently, 2PPE was used in conjunction with (100) surfaces of Cu and Ag to probe image states which were again used as the intermediates and were well within the Cu band gap (Fig. 1).[4,23,25] Since the initial state in this case was a bulk band, the intensity of the signal for this surface was an order of magnitude lower than from the (111) faces for comparable light intensities. In the case of the Cu(110), the 2PPE signal intensity is reduced for two reasons: 1) there is no initial surface state for 2PPE, and 2) the IP system is fully mixed with the bulk continuum, that is, it is an image resonance. Despite this

resultant relatively weak 2PPE signal, we were able to observe the Cu(110) n=1 IP resonance and

measure its position and width.

Figure 2. Our experimental apparatus, which is suitable for high-resolution angle-resolved 2PPE measurements with tunable photon energies in a UHV environment.
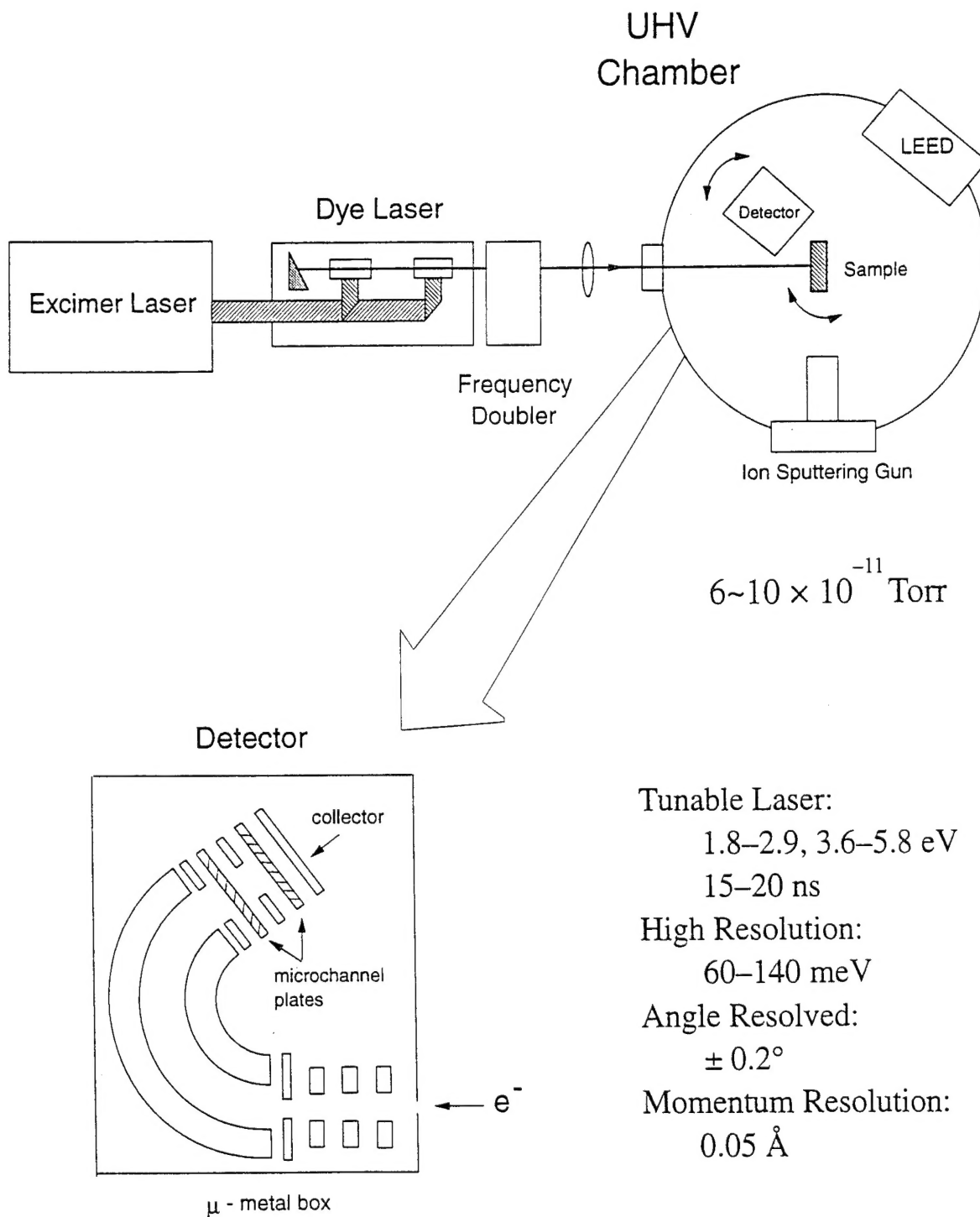
Our experimental apparatus consisted of a pulsed laser and a UHV chamber containing the sample and the electron-energy analyzer (Fig. 2). The light source used in the experiment was a frequency-doubled tunable dye laser pumped by a XeCl excimer laser (λ = 308 nm) with a 15-ns pulse width. The incident light was p-polarized, in accordance with selection rules for transitions considered in our experiment.[26] The angle of light incidence was 68° away from the normal. The intensity of the incident light was sufficiently low that sample heating due to laser irradiation was negligible. Before being loaded into the ultrahigh-vacuum chamber, a (110)-oriented single-crystal copper sample (99.999% purity) was chemically cleaned. The sample was then sputtered (1~2 kV, 5×10^{-5} Torr Argon) and annealed (~800 K) until a sharp $p(1 \times 1)$ low-energy-electron-diffraction pattern appeared. As described below, the work function of Cu(110) was measured using our experimental electron distribution curves (EDC's) as 4.46 ± 0.04 eV, which agrees well with results obtained by other groups.[27] This measurement provided a confirmation of the surface quality, since for contaminated or damaged surfaces a work function change would be expected. During the measurements, the chamber base pressure was typically below 8×10^{-10} Torr. The electron energy was analyzed using an electrostatic, 160° spherical-sector energy analyzer with an acceptance cone of 0.002 steradians. The analyzer resolution was experimentally established from the numerical fits to the image state EDC (discussed below) as 140 meV. Both the energy analyzer and its multichannel plate detector were enclosed in a μ-metal box and biased at 5 V with respect to the sample in order to reduce stray magnetic field distortions of the EDC's. Finally, note that acquisition of the 2PPE IP signal with good signal/noise ratio required numerical averaging of repeated measurements.

1. Non-Image-Potential Features

A typical EDC for normal emission and $h\nu = 4.14$ eV, is presented in Fig. 3. Three peaks appear at 5.8 eV, 7.3 eV, and 9.3 eV kinetic energy. These energy values correspond to the actual kinetic energy values shifted by the difference in the work functions between the sample and the detector as well as by the 5V applied bias.

The peak at 5.8 eV is due to the single-photon photoemission process from thermally excited states just above the Fermi level, in the vicinity of the Σ_1 band (inset Fig. 4), to free-electron-like states above the vacuum level. The high energy tail of this peak arises in part from 2PPE from bulk states 3~4 eV below E_F. The inset of Fig. 3 clearly shows the two contributions to the 5.8 eV peak. This data was taken with higher incident photon energy than in Fig. 3, which caused the 1PPE peak to be enhanced over the 2PPE tail in comparison to the results shown in the figure. Rapid decay of the 1PPE peak, which can distinctly be seen from the inset, reflects an
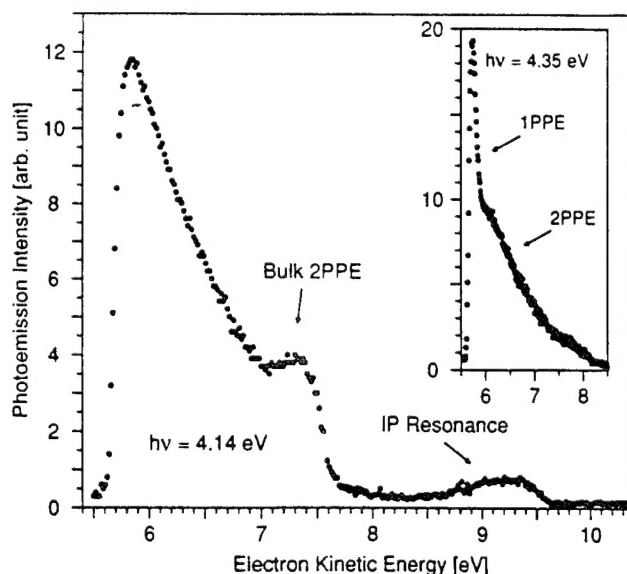

Figure 3. Typical two-photon photoemission energy distribution curve for Cu(110) (normal emission, $h\nu = 4.14$ eV). Single-photon photoemission as well as two-photon photoemission features are observed. The inset shows the 5.8 eV peak scanned at a higher photon energy, $h\nu = 4.35$ eV, for which two components of this peak are clearly distinguishable.

8

equivalent temperature of several hundreds of degrees. The low energy side of the 5.8 eV peak abruptly terminates at the position of the vacuum level, indicating the photoemission threshold. The final shape of the scan is also smoothed due to the limited energy resolution of our electron energy analyzer. In order to determine the energy position of the vacuum level as well as the energy resolution of the electron-energy analyzer, the shape of the peak was modeled as an abrupt step with an exponential decay, convoluted with the expected Gaussian resolution function of the energy analyzer.[28] A least square fit of our data to this model produced the energy location of the vacuum level, which is analogous to the actual 0-eV kinetic energy of photoemitted electrons.

To examine whether space-charge effects were distorting the spectra under the conditions shown in Fig. 3, the EDC was scanned at several light intensities including those smaller than and the same as used in the figure. No substantial change in the shape of the peak was observed confirming that space charge effects were not significant in our observation of Cu(110) image feature. In addition, in the course of our work on this and other experiments it was observed that when space-charge effects were important, shifts in the low-energy cutoff occurred. Care was taken to insure that no such effects were present when obtaining the data.

The small broad peak at 7.3 eV (Fig. 3) stems from 2PPE excitation from a 3d-like bulk band of copper.[29] Figure 3 shows the variation in kinetic energy position of this feature with the change in the incident photon energy. The data lies on a straight line with a slope of 2 ($\Delta E_{kin}=2\Delta h\nu$), which indicates that this feature is due to a fixed initial state. The fact that the EDC signature of this state was also observed on contaminated Cu(110) surfaces establishes that a bulk state is the initial level in this transition, specifically the 3d-like bulk band of Cu.

9

2. Image-Potential Features

The high kinetic energy of the 9.3 eV EDC peak (Fig. 3) indicates that this feature is due to a two-photon process. The position of the rising edge of this peak was monitored as the incident photon energy was varied and it was established that the kinetic energy change of the peak was equal to the change in the incident photon energy. This result indicated that the 9.3 eV feature uses a fixed intermediate state in the two-photon process. The photoemission intensity of this peak was sensitive to the quality of the prepared surface. For example, if Cu(110) was contaminated by a 12 hour exposure to 5×10^{-10} Torr the 9.3 eV feature was not seen; in fact, three sputter/anneal cycles were required to obtain the feature again. Its binding energy (determined below) was in the expected range for a n=1 IP resonance, and an angle-resolved 2PPE study of this state confirmed that it had positive dispersion. Since previous studies have not reported other surface states in this energy range, we concluded that the 9.3 eV feature is due to the IP resonance on Cu(110).
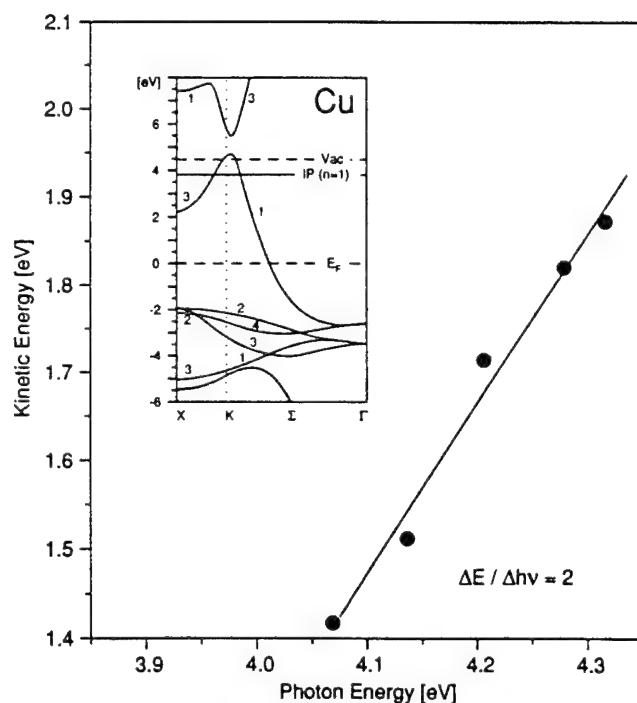
Figure 4. Variation of the kinetic energy of the 3d bulk band peak with change in photon energy. The $\Delta E_{kin}=2\Delta h\nu$ dependence indicates a fixed initial state. The inset shows the bulk energy bands of Cu.[45,47,48]

10

The slope of the high-energy side of the resonance EDC is step-like, reflecting a Fermi energy cut-off, i.e. the rapid decrease of occupied energy states above the Fermi energy level. Figure 5 gives a schematic representation of the 2PPE process for a broadened intermediate state indicating that the final EDC is the product of the actual image-state feature multiplied by the Fermi function. The Fermi cutoff is convoluted with a Gaussian which reflects the resolution of the detector. Note that in this analysis it was implicitly assumed that the density of the initial bulk states about EF is constant, an assumption which is reasonable given the nearly constant slope of the Σ_1 band near E_F (inset Fig. 4).
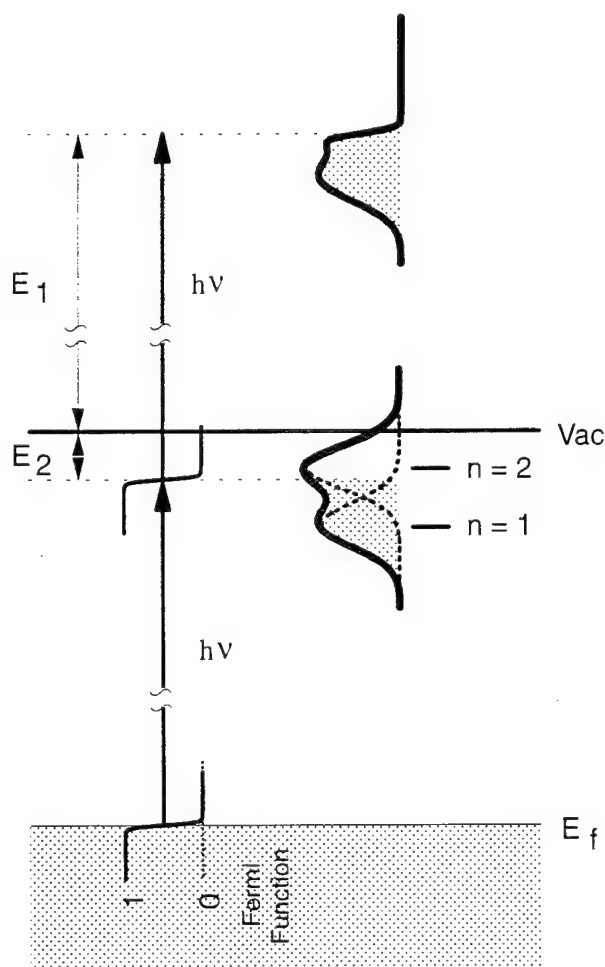
Figure 5. Two-photon excitation process for a broad intermediate state. Due to the Fermi distribution function, the states below $E_F + h\nu$ are predominantly populated by the first photoexcitation. The resultant EDC is a modified signature of the broad intermediate state (in our case, the IP resonance).

11

As is clear from Fig. 5, it is possible, in principle, to measure the entire image-potential feature by increasing the photon energy. In practice, however, as the photon energy was increased, the 5.8 eV peak grew and for $\lambda < 285$ nm (h$\nu > 4.35$eV) significant distortion of the EDC occurred due to space charge. The Cu(110) IP data for $\lambda = 285$ nm (h$\nu = 4.35$ eV) is shown in Fig. 6, where the energy axis is referenced to the vacuum level. Due to the weak photoemission signal under these conditions, it was necessary to average numerically several scans taken at the same emission angle and incident light intensity. During the data collection, no significant change in the work function was observed which confirmed the consistent quality of the examined surface throughout the experiment. In the data of Fig. 6, each data point was effectively sampled 4200 times.
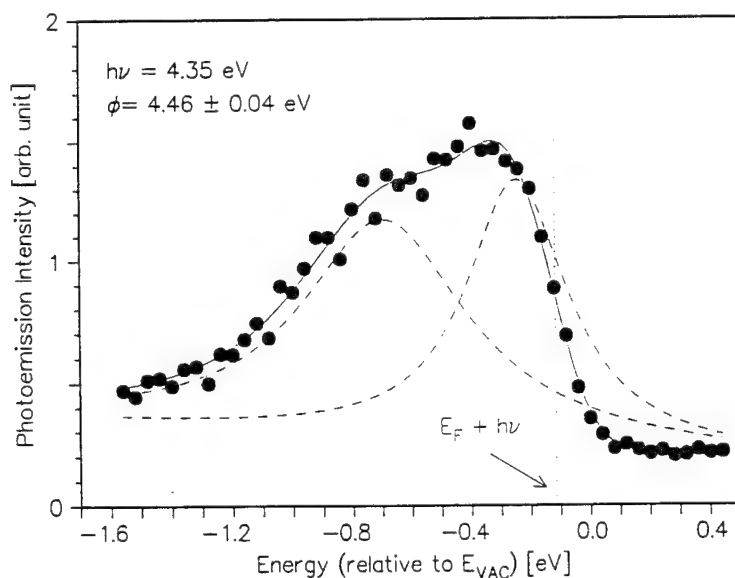
Figure 6. The image-potential-induced EDC peak on Cu(110) (normal emission, h$\nu = 4.35$ eV), composed of two broad, image resonances which have blended into a single feature. The E_F + hν level has been indicated. The resultant work function is $\phi = 4.46\pm0.04$ eV.

The lack of distinctive detail on the low-energy slope of the observed IP feature suggested that the feature was composed of only one energy-broadened IP resonance (n=1). To confirm

this interpretation, a numerical fit to this feature was attempted by approximating it as one Lorentzian with an exponential background multiplied by a Fermi function. Deviation of this fit from the shape of the data was significant, and the numerically determined binding energy of the one Lorentzian differed for fits to different data sets. This inconsistency indicated that the observed feature was composed of at least two overlapping Lorentzian curves (n=1 and n=2) which were broadened due to mixing with isoenergetic bulk levels.

Approximating the IP feature as two Lorentzians with an exponential background multiplied by the Fermi function and convoluted with a Gaussian resolution of our detector, we obtained numerical fits that were very consistent from one data set to the next. The lower energy Lorentzian was assigned to the n=1 IP-induced resonance and the peak of its density of states ("effective binding energy"), referred to the vacuum level, was determined to be 0.68 ± 0.1 eV. The FWHM of this feature was measured to be 0.66 ± 0.06 eV which reflects a lifetime of 1.00 ± 0.09 fs. Lack of detail on the IP EDC feature did not allow for individual resolution of higher image states. The Gaussian resolution of the electron energy detector was established as 140 meV. The cutoff energy $E_F + h\nu$ is indicated in Fig. 6 while the background due to the tail of the 5.8 eV peak (Fig. 3) has been omitted.

Our experiments report the observation of image *resonances*. Extensive theoretical treatments have been reported for the case of the barrier-induced image *states*. In particular, Smith and co-workers,[30-32] and Echenique and Pendry[33,34] have calculated the binding energies of image states using a WKTs-like phase-shift analysis considering both the crystal and image barrier, while Echenique, Flores and co-workers[35,36] reported detailed calculations of expected lifetimes. The latter show that linewidths on the order of 20 meV are expected for n=1 image state if its linewidth is lifetime limited. Subsequent measurements by Schoenlein *et al.*[23] and

13

Giesen et al.[37] on low index fcc metal surfaces showed somewhat shorter lifetimes and thus correspondingly broader linewidths.

In contrast to the thorough theories that address the image states, there is at present no closed theory for the case of image resonances. Several researchers have attempted to formulate the theoretical treatment of image potential resonances,[16,38-41] however, their work requires an assumed or an *ab initio* calculation of the shape of the surface-potential barrier and/or the bulk core potentials, as inner discontinuities in the potentials are required to reflect electrons toward the surface from the bulk. These same analyses have shown that the positions and the widths of the image resonances are very sensitive to the details of the potential features; and that the appropriate selection of the dominant features of the potential-energy surfaces is still not clear. As a result, most of the theories do not address specific metal surfaces, and those that are surface specific, such as calculations for Cu(111), Au(111) and Al(111) by Jurzyszyn,[42] do not treat resonances of (110) surfaces of fcc metals.

Several of the above analyses do, however, provide a gauge of the relative magnitude of the image resonance density of states and their effective binding energies. For example, an approximation to the value of the effective binding energy of the density-of-states peak corresponding to n=1 image resonance on Cu(110) can be made by examining the results of Smith's multiple-reflection analysis at the edge of the band gap. While the quantitative predictions of the multiple-reflection model agree very well with numerous measurements of binding energies of image-potential states, the theory is only suitable to image-potential resonances which lie in the immediate vicinity of the band edge. Thus the approach is not quantitative for many importantresonance systems. For example, in the case of Al(111), where the resonance is 11.04 eV from the gap, and Au(111), where it is 1.11 eV from the gap,[42] the inverse-

14

photoemission experiments measured the image resonance effective binding energies to be 0.54 eV on Al(111)[43] and 0.60 eV on Au(111),[44] while simple application of the multiple-reflection theory predicts the binding energy of 0.85 eV for both when using the phase shift appropriate to the band edge. For our case, the peak in the density of states of n =1 image resonance on Cu(110) lies ~ 0.8 eV (Ref. 45) from the gap, and thus application of the phase-shift theory can be expected to yield only a very rough approximation to the actual value of the binding energy. In fact, the theory gives an effective binding-energy value of 0.38 eV for the n =1 image resonance, where $\phi_c = 0$ was assumed for image resonances below the Shockley-inverted gap near the K point, as is appropriate for the case of Cu(110). This value is considerably below the binding energy of 0.68 ± 0.1 eV observed in our experiment.

Another estimate of the effective binding energy can be obtained using the approach of Lindgren and Wallden.[40] Their computation assumes a corrugation-free jellium solid and thus is not surface specific. Their results show that the density-of-states curve depends sensitively on the depth of the potential discontinuity, V_0, at the surface, where V_0 is the sum of the free-electron Fermi energy plus the work function. Specifically, if the depth is too shallow no oscillations or maxima in the density-of-states curves are seen, whereas, for very large values of V_0, clear maxima are seen with binding-energy values close to 0.85 eV. Since the actual potential surfaces are not necessarily those of even the best *ab initio* values, the calculated effective binding energies must be used only as a qualitative guide. For Cu(110), the work function is 4.46 eV and the free-electron Fermi energy is 7.00 eV, which gives $V_0 \sim 11.5$ eV, which is smaller than for Al(111).

From Fig. 3 of Ref. 40, the estimated binding energy is then expected to be less than 0.50 eV. Again this rough estimate is smaller than the effective binding energy measured in our experiment. Note, however, that most surfaces of fcc metals have V_0 smaller than 20 eV, which

15

precludes this approach from giving an effective binding energy of greater than ~ 0.55 eV, a result clearly at odds with the inverse-photoemission (IPE) experiments cited above. We note that other more exact but surface-specific treatments of image resonances (specifically the treatment of Jurczyszyn[38,42]) show clearly that higher effective binding energies can be obtained. Specifically, the treatment of Jurczyszyn[38,42] predicts binding energies of up to 0.85 eV for the density-of-states peak of $n = 1$ resonance, which is in the range of what we observed.

Finally, we reemphasize that the above are very rough estimates of the values of the effective binding energies which we would expect to see from our surface. A more precise treatment awaits a development of a rigorous theory of image resonances suitable for (110) fcc surfaces.

Our measurements have also determined that the image resonance of Cu(110) exhibits a broad linewidth, which implies a short mean lifetime of this level. Previous theoretical work on image resonances of generic (111) and (100) faces predicted an energy width of $n = 1$ resonance of up to 1 eV,[16,36,39] where measurements of the Al(111) image resonance observed a linewidth of ~ 0.6 eV,[43] and those on Au(111) a linewidth of ~0.4 eV [as determined by us from the fits to the data of Refs. 44 and 45].[47] Similarly broadened linewidths are expected for image resonances of (110) metal surfaces, specifically Cu(110) in our case. Considering that consecutive members of Rydberg-like image-state series are at most a fraction of an eV apart, we conclude that broad image resonances would overlap and blend into each other, producing a single, very broad feature, as observed in our data.

3. Work Function Measurement

An interesting result of the work presented here is that the 2PPE EDC curve provides a

useful method of *in situ* measurement of the work function ϕ, when $h\nu < \phi$. In particular, numerical fits to the data in Fig. 6 fixed with the energy position of the $E_F + h\nu$ line relative to the vacuum level, E_2 (Fig. 5). Using the value of E_2 the work function can be expressed as $\phi = E_2 + h\nu = 2h\nu - E_1$ and for our data $\phi = 4.46 \pm 0.04$ eV, a value which is in agreement with other data in the literature.[27] It is important to realize that the breadth of the IP resonance enabled us to observe clearly the $E_F + h\nu$ level. Thus, such a 2PPE work function measurement is not possible for surface systems with narrow, intermediate states. For the electron-detector resolution used in Fig. 6, the cutoff corresponding to the transposed Fermi function is sufficiently abrupt to give an accurate (up to 0.1 eV) determination of the work function even without the employment of numerical fits. As mentioned earlier, our work function measurement was sufficiently precise that it could be used for monitoring the surface quality throughout the experiment. For example, a sample that had been exposed to 8×10^{-10} Torr of air for ~ 8 hours exhibited a work function difference of about 0.1 eV, and also a reduced image peak, as compared to that seen on a freshly sputtered/annealed sample.

In summary, we have observed a broad EDC feature that corresponded to the $n = 1$ image potential resonance on Cu(110). Instrumental broadening of the Rydberg-like IP resonance series resulted in an overlap of high members of the series which merged into a single. With the measurement of the binding energy of $n=1$ IP resonance ($E_B = 0.68 \pm 0.1$ eV) and its linewidth ($\Delta E = 0.66 \pm 0.06$ eV), we have demonstrated that the observation of energy-broadened surface resonances is possible with 2PPE technique using $\sim 10^{-8}$ s pulses despite the short lifetimes of the resonant states. This is a significant step in the evolution of the 2PPE spectroscopy as a surface resonance probe. Finally, we note that the 2PPE spectroscopy on broadened IP states also

presented a useful and simple method of measuring the work function without recourse to a second hard-UV photoemission source in certain circumstances.

B. On Jellium-like Metal Al

Here we describe the measurement of an image resonance on Al(111) using two-photon photoemission, a resonance system which is particularly important because it has been examined with such care by a series of theoreticians. It provides an excellent model system for comparison of experiments and theory. Thus we compare our experimental value of the binding energy to that obtained by the theoretical treatment of Papadia *et al.*,[41] who predict the image resonance formation for a jellium-like solid with lattice-induced corrugation, and by Jurczyszyn,[38] who utilized a Green's function approach for the treatment of image resonances on (111) fcc metal surfaces.

The measured 2PPE signal originating from Al(111) IP-induced level is expected to be very weak due to the surface and bulk band structure of aluminum. First, as in the case of Cu(110), as there is no surface state to provide a strongly overlapping initial state for the 2PPE process, the population of the IP resonance relies on excitation from the evanescent tails of bulk bands to the surface resonance. The result of a much stronger overlap between a surface state and an image level is shown clearly in the case of Cu(111),[21,22] for example. Second, for Al(111) the IP system is fully mixed with a larger density of states in the bulk continuum. This provides, in effect, rapid "relaxation" path into the bulk for electrons excited to the IP resonance level. Because the IP-induced level is matched against the middle of a wide aluminum bulk band, surface electron reflectivity in this case is smaller than in our previous measurement of the Cu(110) IP resonance, which lies only 0.8 eV from the bulk gap[45] and, therefore, in a region with a smaller

18

density of states. Thus one would anticipate a shorter effective lifetime for an electron trapped in the IP resonance of Al(111) than for the case of the IP resonance on Cu(110); therefore, the 2PPE signal corresponding to the Al(111) IP resonance should be smaller than the already weak 2PPE signal of Cu(110) IP resonance. Despite these considerations we have measured a very weak, but real, 2PPE signal corresponding to Al(111) IP resonance and have determined its energy position.

A typical energy distribution curve for normal emission and for $h\nu = 4.00$eV is presented in Fig. 7. The position of the vacuum level is indicated by zero kinetic energy. The strong emission feature at 0 eV is the result of low-energy electrons from one- and two-photon photoemission processes as described in Section I. The low-energy side of this peak abruptly terminates at the position of the vacuum level, indicating the photoemission threshold.
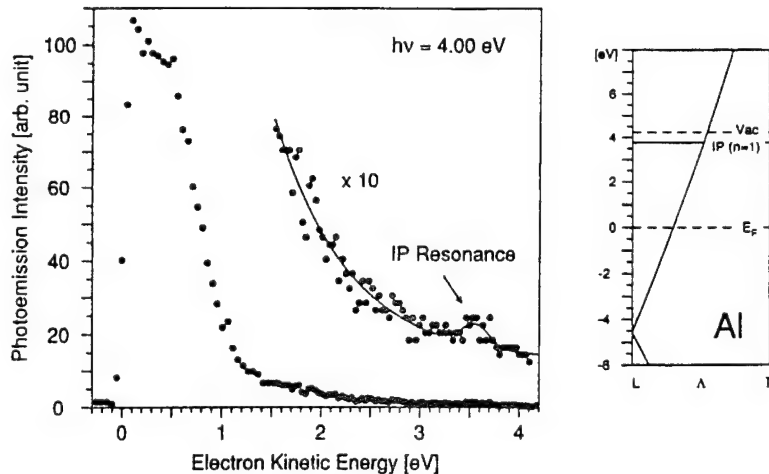

Figure 7. Two-photon-photoemission EDC for Al(111) at normal emission. The inset shows the bulk energy bands of Al.[49]

An expansion of the intensity scale of the EDC in Fig. 7 reveals a small peak at 3.5 eV. Note that despite the small intensity of this 3.5-eV signal, it was clearly observed for numerous

19

EDC scans. Furthermore, the 3.5-eV feature was only observed on well prepared surfaces which identifies its surface, rather than bulk character. The high kinetic energy of this peak indicated that this feature is due to a two-photon process. The nearly constant slope in the bulk energy bands for the Al(111) (Γ-L) direction would suggest that a significant increase in the density of bulk states would not be expected for the energy range corresponding to one-photon excitation leading to the 3.5-eV feature. Similarly, no significant bulk density of states feature was observed at energies below the 3.5-eV peak for two-photon excitation,[26] further suggesting that the observed photoemission signal does not represent a bulk feature. Since previous studies have not reported Shockley or Tamm-like surface states in this energy range, we conclude that the 3.5-eV feature is the IP resonance expected for this surface. EDC scans at several different incident photon energies further confirmed that within the uncertainty of the experiment the observed 3.5-eV feature is a fixed intermediate level. We note, however, that since the observed feature is weak in intensity and located very close to the vacuum level, photon energies which are big enough to populate this level and still small enough to avoid space charge effects, are limited in span to about 0.2 eV. While this tuning range is comparable to the uncertainty in our measurement (0.1 eV) the apparent lack of change in the binding energy is at least consistent with our assignment of the feature as Al(111) image-potential-induced resonance. The low intensity of the 3.5-eV peak did not allow for an accurate measurement of the image resonance linewidth. As a result it was not possible to deduce the work function from the high-energy side of the resonance as was possible in the case of the 2PPE EDC spectra of Cu(110). Instead it was necessary to assume the accepted value of the Al(111) work function of 4.24 eV (Ref. 50) in our binding energy estimates.

Theoretical treatments of both image states and image resonances indicate that the binding

energy of n=2 IP-induced level can be at most 0.21 eV.[33] Thus given the work function of 4.24 eV for Al(111) surface and the incident photon energy of 4.00 eV in our experiment it is not possible to populate significantly the broadened n=2 IP resonance. As a result the observed signal is dominantly composed of the n=1 resonance contribution. A least-square fit to the data was performed by approximating the observed signal as an exponential decay due to the tail of the 0-eV peak with a Lorentzian superimposed on top (Fig. 7). Consistent fits on data sets of several different measurements established the binding energy of the observed feature as 0.46 ± 0.1 eV, with the energy referred to the vacuum level. Despite the noise in the weak photoemission signal we could repeatedly attain a least-square fit with an uncertainty of 0.1 eV in the measured value of the binding energy for our various data sets.

Most of the available theories of IP resonances do not treat different surfaces for the metals considered; however, surface-specific calculations have been performed by Jurczyszyn[38] for the (111) surfaces of fcc metals. Using a Green's function approach Jurczyszyn studied the influence of the crystal-band structure on the energy spectrum and broadening of image resonances. In this treatment, resonances on (111) surfaces of fcc crystals were investigated by varying the matrix element of the crystal potential, V_{111}, while always keeping the vacuum level above the upper edge of the energy gap L_1. This variation in V_{111} influenced the energy spacing between the vacuum level and the upper edge of the energy gap; thus its variation provided a method of changing the coupling between the bulk bands and the IP level. Applying the crystal parameter value appropriate for Al(111) surface in Jurczyszyn's treatment yields the binding energy of 0.464 eV for the peak of n=1 density of states features.[42] This binding energy value agrees with our experimental observations.

Another approach for estimating the effective binding energy is given by Papadia et al.[41]

21

Their computation assumes a jellium model solid ($r_s/a_0 = 2.07$, appropriate for Al) with lattice corrugation described by pseudopotentials, which is not surface-orientation specific. In this treatment, the IP resonances are formed as the electron wave undergoes multiple reflection between the crystal potential reference plane and the surface-barrier reference plane, both of which are situated at the jellium edge. Formation of the IP resonance was shown to strongly depend on the crystal reflectivity r_c. Adjusting the pseudopotential parameters to the measured phonon dispersion curves of aluminum resulted in a binding energy of 0.47 eV for the peak of n=1 density of states feature.

In summary, we have observed a weak EDC feature that corresponds to the n=1 image potential resonance on Al(111). The increased accuracy of our 2PPE measurement allows a more accurate comparison with the presently available theoretical treatments of IP resonances on Al(111). Excellent agreement between our measured binding energy and Jurczyszyn's theory is obtained. Finally, our measurement provides further confirmation for the existence of image potential resonances on Al(111).

II. Image-State Electron Dynamics on Cu(111)

A. Relaxation Channels

Although there have been several studies of the image-state lifetime by means of linewidth measurement[28,51-54] as well as femtosecond time-resolved measurement,[23,55] image-state relaxation dynamics are far from well-understood in terms of relaxation channels and their relative contributions.[37,56] Generally, interactions between the image-state electron and bulk-state electrons are regarded as providing the main relaxation channels; these processes depend on the detailed band structures of that specific surface.[35,36] For such relaxation channels, image-state

electrons of higher quantum numbers, which are further above the surface, should experience less interaction with the bulk and thus are expected to have longer lifetime. Other channels, which are much less studied, include electron-phonon interactions[57] and electron-electron interactions among the image-state electrons themselves. Based upon our measurements at reduced temperatures, electron-phonon interactions do not contribute significantly to the image-state relaxation for bare Cu(111) over the temperature range of 150 - 300 K; however, for the system of Na/Cu(111) at small Na dosage (< 1/100 ML), there is a small, apparent decrease in linewidth at low temperatures, suggesting the electron-phonon interaction plays at least a partial role in the relaxation of the image state.

B. Analysis of Cu(111) Band Structure

We performed preliminary measurements on intraband thermalization of image-state electrons on Cu(111), which rely on the unique band structure of this surface. Figure 8 shows a diagram of dispersion of the G-S surface-state band and the $n=1$ and $n=2$ image-state bands in the vicinity of $k_{\parallel}$ (parallel momentum) = 0. Note that the G-S band has a large energy dispersion[58] with an effective mass of $m^* = 0.47$ m_e while the $n=1$ and $n=2$ bands both have relatively small dispersion ($m^* \sim m_e$ for $n=1$, and $m^* \sim 0.9m_e$ for $n=2$);[22] that is, there is a significant mismatch in the energy dispersion between the $n=0$ G-S surface state and the image states. Thus radiation of a fixed photon energy can only resonantly excite electrons from the $n=0$ to the $n=1$ or $n=2$ state at a certain $k_{\parallel}$ value. For example, a laser pulse of $h\nu = 4.93$ eV will only populate the $n=2$ state from the $n=0$ state at $k_{\parallel} \sim 0.17$ Å^{-1} and not directly excite electrons at $k_{\parallel} = 0$, where photon energy of 5.06 eV is required for the $n=0$ to $n=2$ transition (see Fig. 8). Thus it is possible to selectively excite electrons to higher-energy regions of the image state band without populating those at

lower energy. As a result, the relaxation of image-state electrons from their excited state to lower
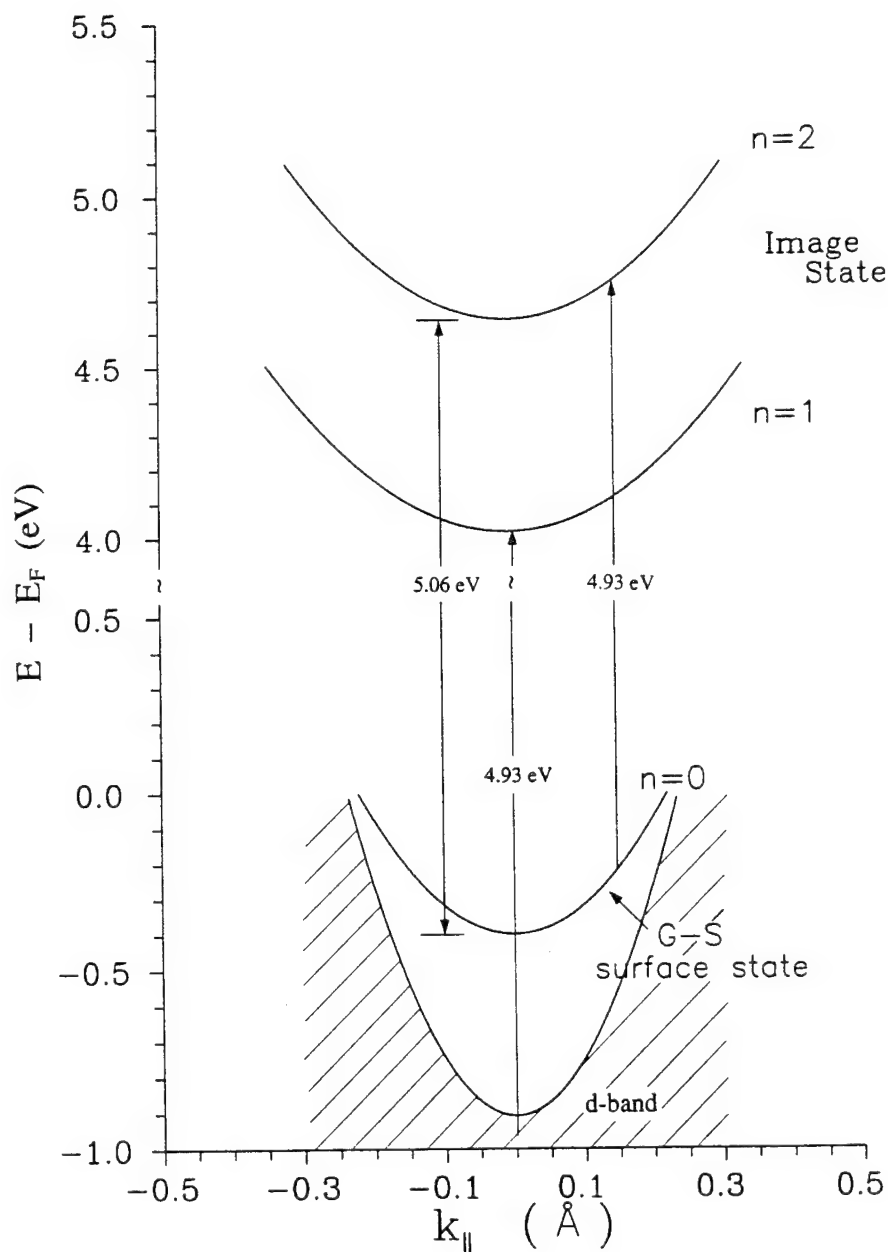
states can be studied.

Figure 8. Band Structure Diagram of Cu(111). Resonant excitation from the n=0 to n=2 states for photon energy of 4.93 eV is obtained at $k_1 \sim 0.17 \text{ Å}^{-1}$.

C. Nonthermal Behavior of Image-State Electrons

Figure 9 shows the 2PPE EDC's due to laser excitation of photon energy of 4.93 eV at different detection angles, where both the n=1 and n=2 states are observed. Here, the n=1 state is populated *via* excitation of the d-band electrons, which has a continuum energy band below the band gap as indicated in Fig. 8. The results show that the signal intensity for the n=1 state is significantly higher at normal emission than at larger emission angles, which is expected because of the higher electron-collection efficiency and longer lifetime at the bottom of the image-state band. However, in contrast to the n=1 state, the intensity for the n=2 state is higher at larger angles than at normal emission, which is clearly a result of the mismatch of the energy dispersion between the n=2 state and the G-S surface state at resonant excitation. More importantly, the behavior of the signal intensity for the n=2 state suggests a nonthermal condition of the image-state electrons prior to ionization.
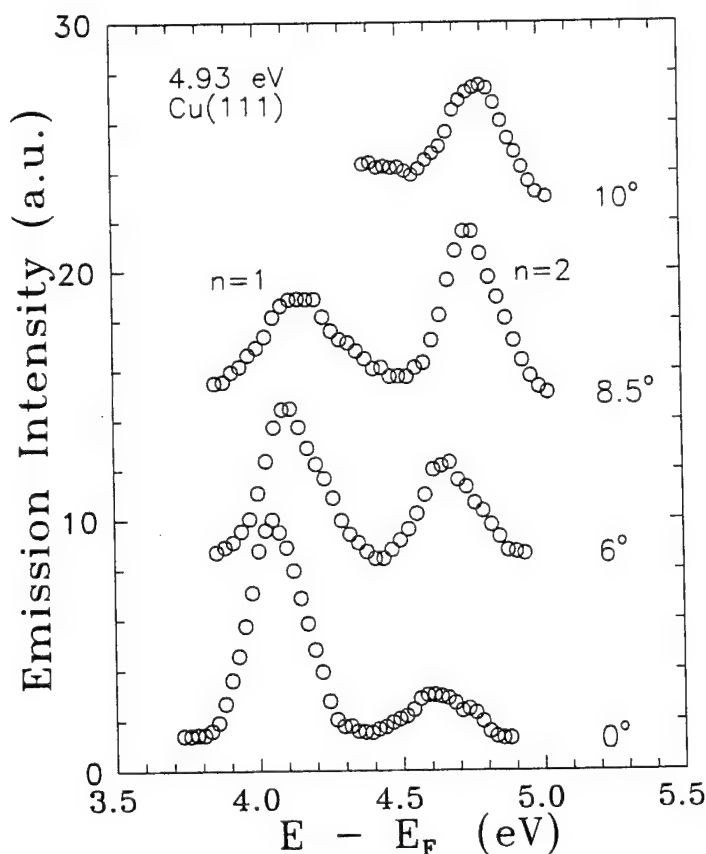

Figure 9. 2PPE spectra of the image states at different detection angles on Cu(111) excited from the n=0 surface state by laser pulses of hν = 4.93 eV.

If image-state electrons did thermalize during laser excitation, one would expect the electrons excited to higher energy to relax to the bottom of the band and hence to display an electron-population peak at $k_\parallel = 0$, $i.e.$, the signal intensity for the n=2 state should always be the strongest at $k_\parallel \sim 0$ (at detection angle $\theta \sim 0°$). Instead, the EDC's in Fig. 9 shows the population peak at the resonant excitation, $i.e.$, at $\theta \sim 8.5°$ (or $k_\parallel \sim 0.17$ Å^{-1}). Note that the 2PPE process here is incoherent (see Section III), thus ruling out any relevant coherent phenomena.

Therefore, the electrons excited simply do not relax to its lowest energy state within the laser excitation pulse. Unlike bulk electrons, which thermalize among themselves within 10^{-13} – 10^{-15}s,[59,60] image-state electrons clearly have much longer relaxation time. This suggests that image-state electrons are lost due to other interactions before they thermalize. A femtosecond time-resolved measurement with the experimental scheme described here using a bichromatic pump-and-probe would further quantify the relaxation time.

III. 2-D Scattering Processes and Confinement on Na/Cu(111) and Other Interface Systems

Two-dimensional (2D) electron systems, including those at single-crystal conducting surfaces[61] as well as at numerous interfaces of interest in semiconductor devices,[62] have been the subject of considerable interest for the last few decades. In recent years, the system of alkali-metal adsorption on a single-crystal metal surface has attracted much attention[63] because of the relative simplicity of its physical phenomena and ease in sample preparation; understanding this simple system can hopefully guide our investigation of more complex solid interfaces. An interesting and analytically tractable excited-state 2D electronic system is that of the image-potential states on highly polarizable surfaces. These states form a Rydberg series with binding energies E_n of typically ≤ 0.85 eV below the vacuum level because of the Coulombic nature of the

26

image barrier.[64] While there have been several studies of image states on alkali-adsorbed metal surfaces, where alkali-induced surface states as well as image states were observed at monolayer alkali coverages,[65] the scattering mechanisms of image-state electrons in such a system have been hardly investigated.

In this section, we report studies of the dynamics of the 2D image-state electron on a single-crystal substrate in the presence of very low coverages (< 1/100 ML) of alkali adatoms. In particular, we focus on an angle-resolved, two-photon photoemission (2PPE) investigation of the scattering of the n=1 image-state electrons by nearly ionized surface species introduced through the adsorption of Na on Cu(111). The 2PPE technique has been proven[64] to be a useful method for observing these normally unoccupied image states because of its high energy resolution. The use of angle-resolved photoemission allows us to study selectively the dynamics of electrons with a given, unique lateral velocity, unlike, for instance, transport-measurement techniques in which the appropriate parameters are averaged over a few kT about the Fermi energy.[66] The interaction of a 2D Fermi gas with Coulombic scattering centers is important in semiconductor interfaces,[67] where it represents one of the main factors limiting electron mobility. By using the angle-resolved 2PPE technique, we can distinguish and characterize two different scattering mechanisms, *i.e.*, the inelastic scattering, where image-state electrons are scattered into bulk states, and the elastic scattering, where nonlifetime features are encountered.

A. Experimental Results

In the first experiment we chose to examine the n = 1 image state on Cu(111). The image state on this surface can be efficiently excited from the well-known Gartland-Slagsvold (G-S) surface state[68] located ~ 0.4 eV below the Fermi level. In addition, because this image state lies

near the top of the projected s-p hybridization gap at k ~ 0, the density of available unoccupied bulk states, which can serve as Auger decay channels for the image state, is low in its vicinity. Thus a strong photoemission signal can be obtained using resonant 2PPE, with the G-S state as the initial state, at relatively moderate UV intensities, permitting us to study the behavior of the image state over a relatively wide range of alkali-metal coverage. The Cu(111) sample (99.999% purity) was mechanically and chemically[69] polished before being loaded in the UHV chamber, and then subjected to multiple sputter (2 kV, 5×10^{-5} Torr of Argon)-anneal (~800 K) cycles until a sharp LEED pattern was observed. The scattering centers were introduced by depositing controlled amounts of Na onto the sample from a well-outgassed commercial getter source (SAES, Inc.). The vacuum condition in the UHV chamber was significantly improved to accommodate the stringent experimental requirements where the vacuum level is very important to the chemically-active alkali-metal adsorbates and other interface environments. The chamber base pressure was typically $\sim 6.5 \times 10^{-11}$ Torr during the measurements, and always $< 1.0 \times 10^{-10}$ Torr during Na evaporation. The experiments were performed with the same excimer-laser-pumped tunable dye laser as described earlier. The frequency-doubled laser pulses of photon energy $h\nu = 4.47$ eV, which is roughly equal to the energy of the resonant transition between the intrinsic surface state and the n=1 image state,[21] were used to excite the image state on Cu(111). The intensity of the incident light was kept low enough to avoid sample heating and space-charge effects. The electron energy-distribution curve (EDC) was analyzed with an electrostatic, 160° spherical-sector analyzer coupled to a pair of microchannel plates and a transient digitizer. The acceptance cone of the detector is about 0.002 sr, giving a momentum resolution ~ 0.05 Å^{-1} for the measurements presented here. The detector energy resolution was improved in the experiment and could be set as high as 60 meV. However, in practice, the detector resolution

was set at ~ 95 meV in order to obtain a good signal-to-noise ratio throughout the experimental range. In the angle-resolved experiment, the incidence angle of the laser pulse was fixed at 68° while the detector was rotated with respect to the sample surface in the incidence plane; the accuracy of this rotation was better than ± 0.2°. The sample was biased − 4.0 V in order to help eliminate the effects of any possible stray magnetic field and space charge.

B. Dramatic Quenching on Image States by Alkali Adsorbates — Coverage Dependence

A typical photoemission EDC from a clean Cu(111) surface at normal emission is shown in Fig. 10. The peak at the low energy is due to electrons photoexcited from the thermal tail of the Fermi distribution by one-photon photoemission (1PPE). The peak at ~ 3.65 eV above the vacuum level, E_{vac} , is due to 2PPE from the n = 1 image state. The binding energy (relative to E_{vac}), E_B = 0.82 ± 0.02 eV, is calculated from (hv − E_{kin}), where E_{kin} is the electron kinetic energy above the vacuum level. Our measured value agrees well with the values given in Refs. 21 and 22. The intrinsic linewidth of the 2PPE peak was determined by fitting the peak with a convolution of the Lorentzian lineshape for the image state and a Gaussian response function of the electron energy analyzer.[53] The Gaussian detector linewidth, Γ_{res}, was set to 95 meV (FWHM), a value which was determined by a measurement of the low-energy cutoff of the 1PPE peak.[51,53] The nonlinear least-square fit of the experimental data and the deconvolution yielded an intrinsic FWHM of Γ = 25 ± 10 meV for the n = 1 image state on Cu(111), in fair agreement with the value Γ = 16 ± 4 meV from previously reported.[53] This approach was verified through a separate technique which measured the n = 1 peak width at different values of detector energy resolution and then extrapolated the linewidth to zero resolution, giving a result of Γ = 20 ± 8 meV. Interestingly, the width of the n = 1 feature was found to be sensitive to the quality of
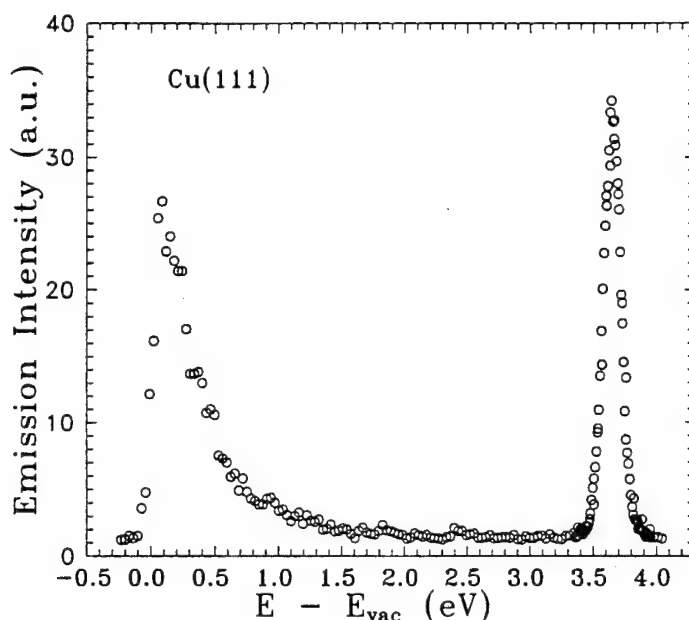
29

surface preparation.

Figure 10. A typical photoemission energy-distribution curve (EDC) obtained at normal emission from Cu(111), excited by laser pulses of 4.47 eV photon energy. The low-energy peak originates from the Fermi tail through a 1PPE process, and the sharp peak at higher energy is due to 2PPE with the $n = 1$ image state as the intermediate state.

The evolution of the image-potential peak at normal emission under conditions of the same excitation intensity on the Cu(111) surface at Na coverages, from $\Theta = 0$ to $\Theta = 9/1000$ ML, is shown in Fig. 11. The Na deposition on Cu(111) was monitored by the alkali-induced change in work function. At low coverages the adsorbed atoms are highly polarized[63] normal to the surface, forming electric dipoles that dramatically decrease the dipolar portion of the bare-surface work function. The work function change is measured from the shift in the low-energy cutoff of the 1PPE peak. The amount of Na coverage is then calibrated against a previously reported[70] work function-vs-coverage curve for Na on Cu(111). These results can be independently verified by separate coverage-dependent LEED measurements. Specifically, we observed the characteristic disordered overlayer structure throughout the low coverage range ($\leq 1/100$ ML), followed by the gradual development of a ring-like diffraction pattern at higher coverage, until

finally an ordered (3/2×3/2) hexagonal Na adsorption structure appeared at a coverage of about
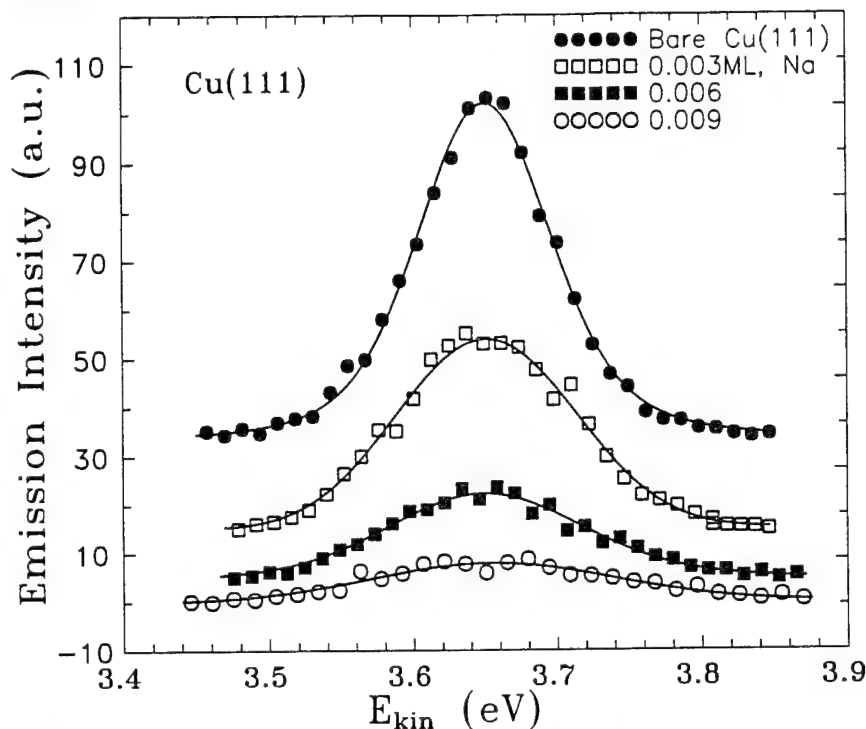
0.4 ML, consistent with results described in Ref. 70.

Figure 11. EDC's from the n = 1 image-state at normal emission from Cu(111) in the presence of Na adsorbate, at coverages of Θ = 0, 3/1000, 6/1000, and 9/1000 ML, respectively. The fit to the data was obtained by a convolution of a Gaussian and a Lorentzian lineshape as described in the text, using a nonlinear least-square algorithm.

Figure 11 shows a sharp decrease in the photoemission intensity upon Na adsorption; in

fact, at a coverage as low as 0.012 ML, the image state appeared to be completely quenched. In

addition, the image peak was significantly broadened with Na coverage. Also note that the

energetic position of the peak does not appear to shift with coverage, even though the work

function, as measured from the low energy cutoff of the 1PPE peak, does decrease significantly

with Na coverage, e.g. ~ 0.35 eV at a coverage of 0.009 ML. (Any energy level shift observable

is gauged against the constancy of the detector contact potential.) This result suggests that the

observed image state exists only in bare regions of the surface where the effect of the Na-

adsorption-induced dipoles on the work function is minimal. In these regions, the "local"

workfunction[71] is the same as on the clean surface; in contrast, the experimentally measured work function is a value averaged over a macroscopic area of the inhomogeneously covered surface. Since image states are energetically "pinned" to the vacuum level,[4] photoelectrons from the image state are thus detected at the same kinetic energy as from the bare surface.

C. Momentum-Resolved Measurements on 2D Scattering and Confinement

1. Effective Mass Measurement and Conservation of Electron Lateral Momentum

In order to characterize the quenching and linewidth broadening mechanisms shown in Fig. 11, we performed an angle-resolved 2PPE study. A typical angle-resolved EDC spectrum is shown in Fig. 12 for the bare Cu(111).
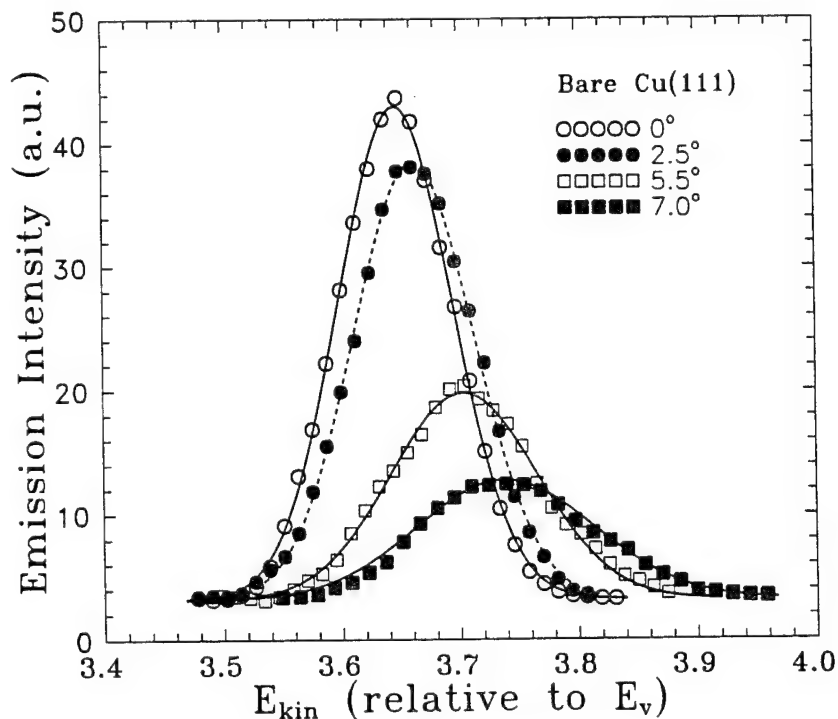

Figure 12. Typical angle-resolved 2PPE spectra for the n=1 image state of bare Cu(111).

32

First, the dispersion curve for the image-state band was measured since information on the effective mass of the n = 1 image state is needed for the linewidth analysis. The angle-resolved detection system, at a fixed bias, was first calibrated against the well-known dispersion relation for the n = 1 image state on Cu(100).[25] For Cu(111), the data are shown in Fig. 13.
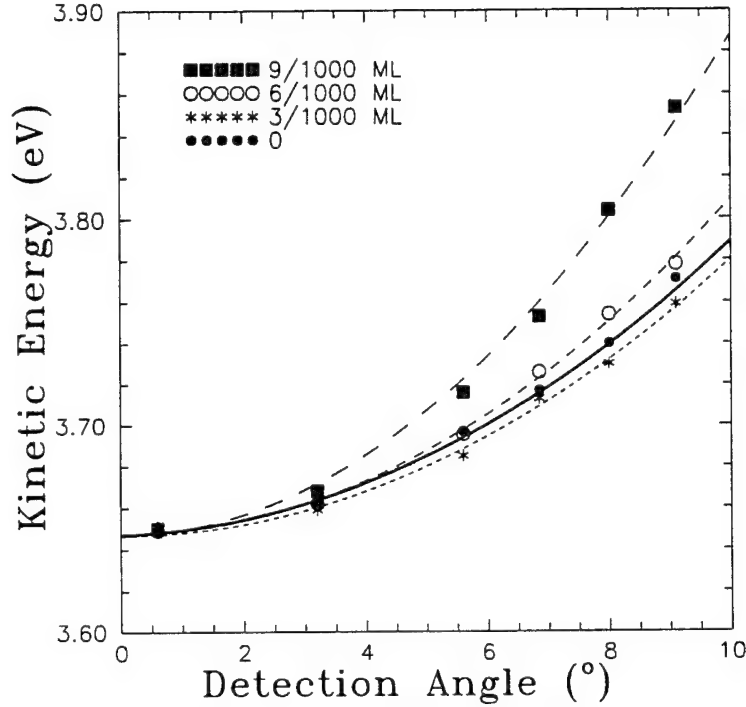
Figure 13: Energy dispersion distributions of the n=1 image state on bare and Na-covered Cu(111), at coverages of Θ = 3/1000, 6/1000, and 9/1000 ML, respectively.

For the clean Cu(111) surface, the fitted parabolic curve using $E_{kin} - E_{bias} = (h\nu - E_B)$ $[1+(m_e/m^*)\sin^2\theta]$ gives an effective mass $m^* = (1.0 \pm 0.1)m_e$, which is in good agreement with other observations,[22] and where E_{kin}, E_{bias} and E_B are the detected kinetic energy and bias potential energy, and binding energy of the image state, respectively. For the case of Na adsorbed Cu(111) surfaces, the measurements yield values of effective masses that are nearly the same as that of the bare surface, except for an apparent ~20% decrease seen in m^* at Θ = 0.009 1/100 ML. In order to simplify the analysis described below, we have taken $m^* = m_e$ throughout the range of Θ investigated. However, we do note in passing that a similar reduction in effective

33

mass has been seen for image-state electrons upon adsorption of a monolayer of xenon or heavy organics on Ag(111); in these cases the effect was attributed to the screening of the interaction of the image-state electrons with the bulk states by the adlayer.[9,54] Further investigation of the apparent reduction seen at $\Theta \sim 1/100$ ML is planned.
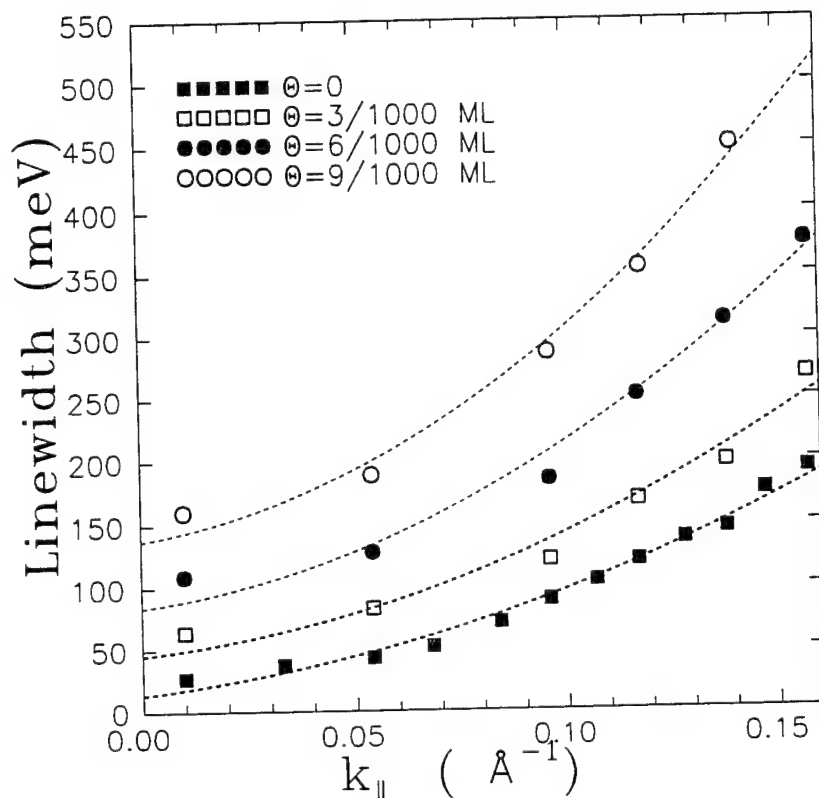
Figure 14. The image-state (n=1) linewidth broadening as a function of the electron momentum parallel to the surface, $k_\parallel$, on clean and Na-adsorbed Cu(111), at coverages of Θ = 3/1000, 6/1000, and 9/1000 ML, respectively.

The broadening of the image-state linewidth as a function of electron momentum parallel to the Cu(111) surface is shown in Fig. 14 for the clean surface and for different Na coverages. Note that in the photoemission the parallel component of the wavevector is conserved before and after the electron is emitted from the surface. This unique and important feature allows a measurement of the momentum of image-state electrons, *i.e.*, the electron momentum can be

described by the parallel component of the emitted electron's wavevector, $k_{\parallel} = [2m_e E_{kin}/\hbar^2]^{1/2}\sin\theta$, where θ is the detection angle relative to the surface normal. The Lorentzian natural linewidths shown were derived based on numerical deconvolution of the measured peak widths using the known detector Gaussian lineshape, as described earlier. The linewidth is clearly seen to increase with $k_{\parallel}$ as well as Na coverage Θ, in all cases. At a given coverage, the relation between the linewidth Γ and $k_{\parallel}$ appears to be parabolic. With higher Θ, the parabolic curvature becomes steeper. The basic trend of linewidth broadening as a function of $k_{\parallel}$ is similar to prior observations in the intrinsic linewidth broadening of the G-S surface state,[58,72] both for the case of unintentional surface imperfections and for dosed K-adsorbate atoms.

2. Contributions to Linewidths of Image States and Electron Scattering

The contributions to the measured linewidth can be analyzed as follows. First, since 2PPE involves three levels, initial, intermediate, and final, the measured linewidth for the process can in principle involve contributions from all three states. However, the measurement involves only the intermediate image state because the 2PPE process is not coherent,[53] *i.e.* the electron loses its phase correlation at the intermediate state due to elastic scattering before being photoionized by the second photon. Normally, in the one-photon photoemission (1PPE) process, the lifetime-limited linewidth of the emitted electron is a linear combination of the linewidths of the initial and final states, *i.e.*, $\Gamma = \alpha\Gamma_{\text{initial}} + \beta\Gamma_{\text{final}}$, where α and $\beta > 0$ and their magnitudes depend on the details of the band structure and the method of the measurement.[73] For the initial state being a surface state, $\alpha = 1$.[53,73] In the 2PPE process, there are three states (initial, intermediate, and final states) involved in the emission. If the whole 2PPE process is coherent (like the 1PPE process), the measured intrinsic linewidth is, in general, a linear combination of the lifetime widths of the

35

initial, intermediate and final states. If the intermediate state (the image state here) is a surface state, thus possessing no dispersion in the direction normal to the surface, the contribution from the final-state linewidth is eliminated; in this case the measured linewidth would be a combination of the initial surface state and the intermediate state linewidths. However, the measured width,[53] using the 2PPE technique, of the image state on a clean Cu(111) surface is always much narrower than the width (≥ 60 meV) of the initial surface state,[72,74] contradictory to the principle mentioned above. The electron has a long enough lifetime at the image state and undergoes elastic collisions to lose the characteristic of its initial state before being photoionized to the final state. Therefore the excitation steps are not coherent, *i.e.* not a simultaneous two-photon process, which is also evident in a recent femtosecond 2PPE experiment.[75] Hence, the linewidths measured here are readily interpreted as those solely of the image state, without complications from the initial and final states.

Broadening of the image-state linewidth can be attributed to both lifetime and nonlifetime effects. The lifetime-related linewidth involves the decay of image-state electrons into empty bulk states, as well as inelastic scattering from defects, "intrinsic" impurities, and intentionally introduced Na scattering centers, whether neutral or ionic. This reduction in lifetime has a direct impact on the image peak intensity, since the image-state electron signal is directly proportional to the average number of electrons in the image state during the laser-excitation pulse. Clearly, the signal intensity from the 2PPE process is also directly related to the population of the initial surface state, which on the bare surface is fully occupied due to its location well below the Fermi level. However, an earlier experiment[72] using one-photon photoemission showed that the adsorption of alkali metal has little effect on the occupancy of this surface state at low alkali coverages such as used here, e.g., < 1/100 ML. Therefore, any change in the 2PPE signal

intensity (integrated) for the measurements presented here can be attributed solely to lifetime changes associated with the image state. Thus, for example, a factor of two increase in lifetime broadening would then imply a factor of two reduction in the measured total signal. In the case of nonlifetime broadening, which is a result of the elastic scattering process, the number of electrons in the image state or the total signal from the 2PPE EDC would not vary with changes in broadening. Therefore, it is possible, in principle, to make an assessment and separation of the contributions from the lifetime and nonlifetime mechanisms by analyzing the reduction in signal intensity in connection with the corresponding linewidth broadening. By numerically integrating the area under the EDC's shown in Fig. 11, the relative image-state signal was found to be $S_1 : S_2 : S_3 : S_4 = 4.1 : 3.0 : 1.5 : 1.0$ for Na coverages of 0, 3/1000, 6/1000, 9/1000 ML, respectively, obtained under the *same* excitation conditions (including the laser incidence angle and intensity on the sample). The corresponding linewidth broadening is $\Gamma_1 : \Gamma_2 : \Gamma_3 : \Gamma_4 = 1.0 : 3.1 : 5.6 : 8.4$ (see Fig. 14 at $\Theta \sim 0$). Since any reduction in the total emission signal depends solely on the shortening of the lifetime, the contribution from inelastic scattering is approximately equal to the nonlifetime contribution; each contributes ~50% to the total broadening for the image state at $k_\parallel = 0$.

The nonlifetime broadening comes from weakened conservation of momentum $k_\parallel$ caused by elastic-scattering processes and mediated by surface defects or, alternately, impurities. This scattering results in electron confinement, thus mixing states of different lateral momenta. As a result, photoelectrons from each scattered image-potential state are emitted over a range of parallel wavevectors, $k_\parallel$, so that a 2PPE peak detected along any given angle is comprised of electrons over a range in energy, resulting in a nonlifetime broadening of the linewidth. Nonlifetime broadening of a surface state has been observed and analyzed by Kevan and Tersoff[58]

37

in relation to angle-resolved photoemission from the G-S surface state on Cu(111), where the linewidth of this state would diminish as the surface band disperses upward towards E_f — if $k_\parallel$ was truly conserved. In fact, they observed an increase in linewidth broadening as $k_\parallel$ increased, similar to the observations shown in Fig. 14 for the case of image states. In their treatment,[58] the finite width in the momentum space, $k_\parallel^s$, of the elastically scattered states can be taken to be equal to the inverse mean free path for intraband scattering,

$$k_\parallel^s = \sigma\Theta/\Omega \qquad (1),$$

where s is the scattering cross-section for these processes, Θ/Ω is the surface density of scattering centers, W the area of the substrate surface unit mesh, and Θ the coverage in monolayer. This expression implicitly assumes that scattering is isotropic.

Finally, the measured linewidth must also include the effect of detector momentum resolution, $k_\parallel^{res}$, in addition to the consideration of its energy resolution. The total momentum broadening to the linewidth can be written in the notation of Ref. 58 as,

$$\Gamma(\Delta k_\parallel) = E(k_\parallel + \Delta k_\parallel/2) - E(k_\parallel - \Delta k_\parallel/2) = \hbar^2 k_\parallel \Delta k_\parallel/m^* \qquad (2),$$

where $\Delta k_\parallel = \Delta k_\parallel^s + \Delta k_\parallel^{res}$. Rigorously speaking, Eq. (2) is valid only when $k_\parallel > k_\parallel/2$. For $k_\parallel \sim 0$, the electron lateral kinetic energy at the detector is nonzero because of the finite $\Delta k_\parallel$ and the measured linewidth at $k_\parallel \sim 0$ is then given by $\hbar^2(\Delta k_\parallel)^2/2m^*$. When all of the contributing factors mentioned above are combined, an expression for the measured linewidths, as shown in Fig. 14, is obtained for $k_\parallel > \Delta k_\parallel/2$,

$$\Gamma = \Gamma_{lifetime} + \Gamma(\Delta k_\parallel) = \Gamma_{lifetime} + \hbar^2 k_\parallel(\Delta k_\parallel^s + \Delta k_\parallel^{res})/m^* \qquad (3),$$

where $\Gamma_{lifetime}$ is the contribution from inelastic scattering events and is lifetime-related, and where Lorentzian widths are assumed for both $\Gamma_{lifetime}$ and $\Gamma(\Delta k_\parallel)$. In this expression the second term (nonlifetime-related) clearly exhibits both $k_\parallel$ and Θ dependence. In general, the possibility that $\Gamma_{lifetime}$ is also dependent on $k_\parallel$ as well as Θ should be considered. Indeed, our angle-resolved data on *bare* Cu(111) show that the *integrated image-state signal* does decrease parabolically with increasing $k_\parallel$, indicating that $\Gamma_{lifetime}$ is in fact $k_\parallel$ dependent. This lifetime broadening, as determined from the signal reduction in the EDC data as a function of $k_\parallel$, contributes about 1/3 of the total broadening shown in Fig. 14 for $\Theta = 0$. However, in the case of Na adsorbed Cu(111), a similar analysis shows only an insignificant lifetime broadening as a function of $k_\parallel$, and hence $\Gamma_{lifetime}$ can be regarded as k independent in the following analysis.

3. Lateral Confinement Due to Elastic Collision and Its Scattering Cross-Section

Using Eq. (3), we numerically fit the Γ-vs-$k_\parallel$ data shown in Fig. 14, using the experimental detector momentum resolution of $\Delta k_\parallel^{res} = 0.05$ Å^{-1}. The least-square fitting shows $k_\parallel^2$-dependent broadening at the four Na coverages of Fig. 14. Elastic scattering occurs both through the controlled surface-Na species and through "intrinsic" impurity and defects unrelated to Na adsorption, denoted by the factor $\Delta k_\parallel^o$. Therefore, one can write,

$$\Delta k_\parallel^s = \Delta k_\parallel^o + \Theta\sigma/\Omega \tag{4},$$

where $k_\parallel^o$ is given by the broadening at $\Theta = 0$, *i.e.*, $k_\parallel \Delta k_\parallel^o = 0.4 k_\parallel^2$. Equation (4) can be used to obtain a Na-induced scattering cross-section $\sigma = (83\pm16)\Omega k_\parallel$, valid for all three Na coverages. This empirical expression indicates a direct proportionality with the parallel momentum for the scattering cross-section of image-state electrons. This result does not appears to be in accord

39

with conventional Coulombic scattering theory, which would suggest that the scattering cross-section should be inversely proportional to $k_\parallel$.[76] However, the elastic scattering process involved here results in the mixing of quantum states, rather than a simple Coulombic-type scattering event, thus deviation from a Coulombic scattering cross-section may be anticipated. Note that for $k_\parallel =$ 0.1Å^{-1} and $\Omega = 5.7$Å^2 for the Cu(111) surface,[77] we find $\sigma = 47 \pm 9$ Å , which is about an order of magnitude larger than the value found for the broadening of one-photon EDC's from the G-S surface state on K-covered Cu(111), using angle-resolved photoemission.[72]

Other experiments have measured linewidth broadening effects only at normal emission. For comparison in our experiment, at $k_\parallel \sim 0$, a nearly linear relation is found between image-state linewidth and coverage with a slope of about 12 eV/ML. This value is significantly larger than that reported for the O/Ni(100) system, with a coverage-dependent broadening of 1.2 eV/ML.[53] Recent studies of image states in the Ag/Cu(111) adsorption system[56] offer an interesting contrasting system. In such a noble-metal adsorbate system, the Cu(111) n = 1 image state does not exhibit significant quenching and broadening until ≥0.6 ML coverage, at which point the *Ag-induced* n = 1 and n = 2 image states become prominent and remain so until they dominate for Θ ≥ 1 ML. The lack of strong broadening effects in this case is in contrast to the fact that alkali-metal adsorbates give rise to particularly strong induced-dipole moments; such a polarized adsorbate would be expected to be a particularly efficient scattering center for lateral confinement and inelastic lifetime quenching.

Preliminary studies have been performed on the n = 2 image-state at photon energies close to the energy difference between the G-S surface state and the n = 2 state. The experiment shows quenching and broadening of nearly the same magnitude as for the n = 1 state. This is not an unexpected result, since an image-state electron in either the n = 1 or n = 2 state is approximately

an equal average distance from a Na-induced dipole, for the low coverages used here. In particular, for the maximum coverage used, $i.e.$ ~ 0.01 ML, the average interatomic spacing is ~ 30 Å, a value much larger than the average distance from the surface for n = 1 and n = 2 of ~ 2 Å and ~ 10 Å, respectively.[78] Experiments were also performed on other systems, such as Cs and Na on Cu(100), and the findings are basically in accord with the Na/Cu(111) system.

In summary, we have performed angle-resolved 2PPE measurements of image-state electron scattering on alkali adsorbed Copper surfaces. The measurements show drastic quenching and broadening effects on the image states at very low alkali dosage (< 1/100 ML) in comparison with other adsorption systems. The nonlifetime linewidth broadening shows significant lateral confinement of the image-state electrons by the introduced alkali scattering centers through elastic collisions. An empirical scattering cross-section is obtained and found to be proportional to the parallel momentum of the image-state electron. This 2PPE momentum-resolved technique can be widely applicable to other simple interface systems in studying 2D excited-state electron scattering mechanisms.

IV. 1-D Confinement and Lateral Superlattice Effects on Stepped Copper Surfaces

In this section, we report the first observation of lateral superlattice effects on a stepped Cu(001) surface using angle-resolved 2PPE of image-state electrons. This measurement was done in conjunction with Richard Haight and Franz Himspel at IBM T. J. Watson Laboratory.

Low-dimensional surface systems have attracted much attention recently because of their fundamental and technological implications. Traditionally, work in these systems has utilized either two-dimensional confinement,[79] $viz.$ the s-p surface states on single-crystal copper or that available at heterojunctions in electronic devices,[62] or for lower dimensionality, through

41

lithographic patterning of 'wires' or 'dots' on single-crystal surfaces.[80] Metallic systems with spacer-layer structures have been seen to possess quantum-well states[81] and display effects of oscillatory magnetic coupling[82] as seen in superlattices with potential applications in magnetic storage.[83] Recently, however, several groups have shown that such low dimensions can be effectively realized and utilized in metals[12,13,84-87] *via* the use of the natural atomic-scale features in vicinally cut surfaces, such as the stepped surfaces created by a small-angle miscut from a low-index plane on a single-crystal metal.[88] Electrons affected by these small features have been shown to exhibit a rich variety of standing-wave[13] and scattering phenomena[86] and lateral confinement of surface electrons.[85,87]

In a recent paper,[85] it was shown that electrons in image states on the surface of a stepped single-crystal metal exhibited electron localization characteristic of one-dimensional (1D) systems. In this case evidence for an isolated step-induced image state was reported, where the electron movement perpendicular to the steps was believed to be confined by the potential trough at the step edge; as for all image states, the dimension perpendicular to the metal surface is confined by the Coulombic image potential and the crystal barrier. Here, we report the use of angle-resolved two-photon photoemission (2PPE) for the direct measurement of a surface lateral superlattice on stepped Cu(001). Our results show that the lateral periodicity (~11Å) of the bare stepped surface leads to back-folding of the dispersion of energy versus parallel momentum, $k_\parallel$, of the image state. Further decoration of the step edges with Na atoms sharpens this characteristic dispersive behavior to the point that it can be followed to the edges of the lateral Brillouin zone formed by the step lattice. The reduction of the surface Brillouin zone by a factor of 4.5, compared to that of planar Cu(001), allows a clear observation of back-folding of the free-electron-like dispersion which is normally seen on planar surfaces, yielding an oscillatory dispersive behavior where the

42

electron energy is a multivalued function of $k_\parallel$ in the first two Brillouin zones of such a superlattice. This observation demonstrates a classic example of the 1D quantum nature that can be described by a simple Kronig-Penney model for electrons in a regular periodic potential.[89] Although the effects of the additional reciprocal lattice vector from the step lattice are known in LEED measurements,[88] they have not been seen previously in the electronic structure to our knowledge.

A. Sample Selection and Preparation

In the experiment we chose to examine a single-crystal copper surface with a 9.5° miscut to the (001) plane where monatomic steps are formed along the [110] direction. On flat Cu(001) it is well known that a regular progression of stable image states is formed since the vacuum level is coincident with the middle of the projected band gap.[25] Because the energy of the image state is located in the band gap around the $\overline{\Gamma}$ point in the k-space for Cu(001), complications due to the interaction of the image-state electron and bulk-state electrons are minimal. While these states are somewhat more difficult to see than in the case of the Cu(111) surface where strong resonant initial-state excitation is possible,[22] the nonresonant nature of the initial state also eliminates masking effects due to initial-state excitation.

The stepped Cu(001) sample was mechanically and electrolytically polished[85] before being loaded in the UHV chamber, and then subjected to multiple sputter (500-1000 V, 2×10^{-5} Torr of Argon)-anneal (~ 800 K) cycles until a well defined split LEED pattern was observed. Sputtering was done along 30° from grazing incidence, in accord with previous studies.[85] The step-edge decoration was accomplished by depositing controlled amounts of Na onto the sample from a well-outgassed commercial getter source (SAES, Inc.). The chamber base pressure was typically ~ 8×10^{-11} Torr during the measurements, and always < 2×10^{-10} Torr during Na evaporation. The details of Na

dosage calibration can be found in Section III. The surface quality was monitored by LEED measurements. The experiments were performed with 17-ns, p-polarized laser pulses generated from a 3-stage excimer-laser-pumped tunable dye laser. The frequency-doubled laser pulses of photon energies $h\nu = 4.4 - 4.6$ eV were used to excite the image state on Cu(001); this photon energy range is sufficient to follow the dispersion of energy versus $k_\parallel$ over a significant portion ($0 \leq k_\parallel \leq 0.4\text{Å}^{-1}$) of the surface Brillouin zone. The data shown here were taken at 4.43 eV. In the angle-resolved experiment, the laser incidence was *fixed* at ~ 68° while the detector was rotated within the incidence plane which is perpendicular to the steps. The sample was mounted so as to allow simultaneous observation along both the [$\bar{1}$ 10] and [1 $\bar{1}$ 0] directions ('uphill' and 'downhill' relative to the step, respectively) of the sample without removing and remounting the sample. The sample was biased at −4.0 V in order to help eliminate the effects of any possible stray magnetic field or space charge. Before making measurements on the stepped surface, a separate planar Cu(001) sample as well as the reverse side of the stepped sample, which was a flat (001), were examined *via* 2PPE and found to display the usual n=1 and n=2 image states reported previously.[25]

B. Measurements on Bare Vicinal Cu(001)

On the miscut Cu(001), a clear split LEED pattern was observed — indicating its step morphology. However, the somewhat diffuse spots suggested a certain degree of irregularity in step spacing. An analysis[88] of the LEED pattern gave a terrace width of d = 11 ± 1 Å which is in good agreement with the intrinsic terrace width of 4.5 rows of the [110]-oriented atoms for this Cu(1$\bar{1}$9) vicinal surface, $D_o = 4.5 \times (a / \sqrt{2}) = 11.5$ Å, where a is the lattice constant of copper lattice. On this surface, the n=1 image state could again be clearly observed; however, its intensity was significantly lower than that for the planar surface. The width of the feature was

44

~70% larger than that seen on the planar surface, a result which is in accord with the scattering of image-state electrons from step edges. In addition, observations of the low-energy cutoff of the EDC from 1PPE measurements indicated that the work function on this surface was generally comparable to the 4.63 eV value measured for the planar surface.
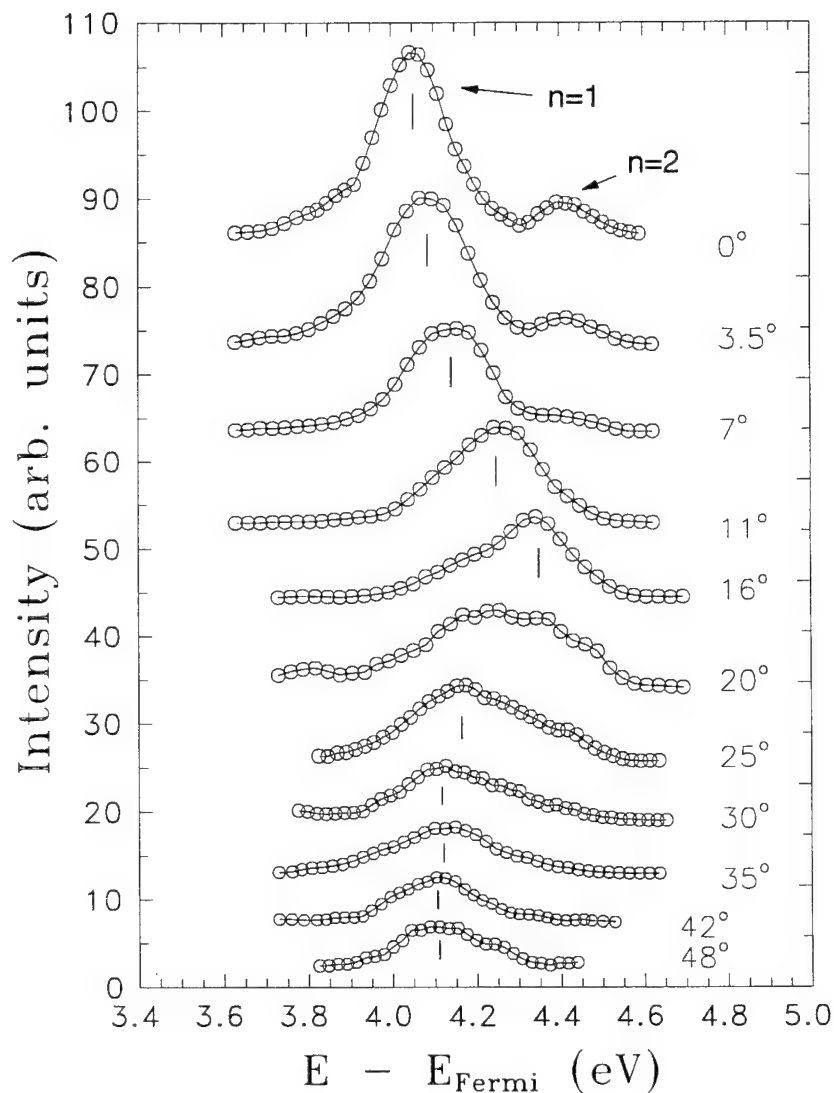

Figure 15. Angle-resolved two-photon photoemission spectra of image states on stepped Cu(001) in the plane perpendicular to the step edges.

Angle-resolved photoemission was then measured towards the $[\bar{1}10]$ direction (in the plane perpendicular to the steps). The data are shown in Figure 15 for detection angles θ from 0 to 48°. They show one feature having parabolic, free-electron-like dispersion, which becomes unobservable beyond $\theta \approx 16°$. A second feature with much smaller dispersion appears near the bottom of the band at ~ 4.1 eV above the Fermi level. Note that for the case of Cu(001), the image state remains in the gap of the projected bulk bands for the parallel wavevector $k_{\parallel}$ of values up to ~0.8 Å^{-1},[90] thus enabling a clear measurement of the image-state dispersion throughout this range of $k_{\parallel}$ (or angle). The results shown were also clearly characteristic of the stepped surface. If the sample was oriented so that the step were 90° to the orientation in the figure only the dispersive n=1 image state was seen.[85] Note that there was no detectable change in the binding energy of the image state from planar to stepped Cu(001). Although it is not shown in Fig. 15, a small peak at ~ 3.65 eV (about 200 meV lower than the main n=1 image-state peak at normal detection) was occasionally detectable at detection angles 0° ~ 7°. This might be accounted for the step state observed in Ref. 85. This step state was seen very sensitive to the stepped surface condition and signal from this state was too weak in our case to make a statement on its nature.

C. Measurements on Alkali Adsorbed Vicinal Cu(001)

The addition of even small amounts of alkali-metal atoms to a metal surface is known to affect greatly the local surface potential and structure. On stepped surfaces, alkali adatoms are most likely to adsorb at the step edges;[91] and the resulting strong alkali-induced dipole repulsion would be expected to lead to step repulsion and more regular and stable steps.[63,88,92] These considerations led us to conduct measurements on a Na-dosed surface. In fact, after low dosage (~ 0.01 ML) on the stepped Cu(001), the LEED pattern sharpened significantly, *i.e.*, about a

factor of two reduction in spot width. The split-spot spacing remained the same as before. Adsorption of sodium to metal surfaces is also known to alter the work function significantly,[16] e.g., $\Delta\phi = -0.2$ eV for ~ 0.01 ML. However, since the energies of image states are known to be determined by the *local* work function,[7,10] the energetics of image states on the terraces would not be affected simply on the basis of macroscopic work-function changes — if adsorption occurred at step edges.
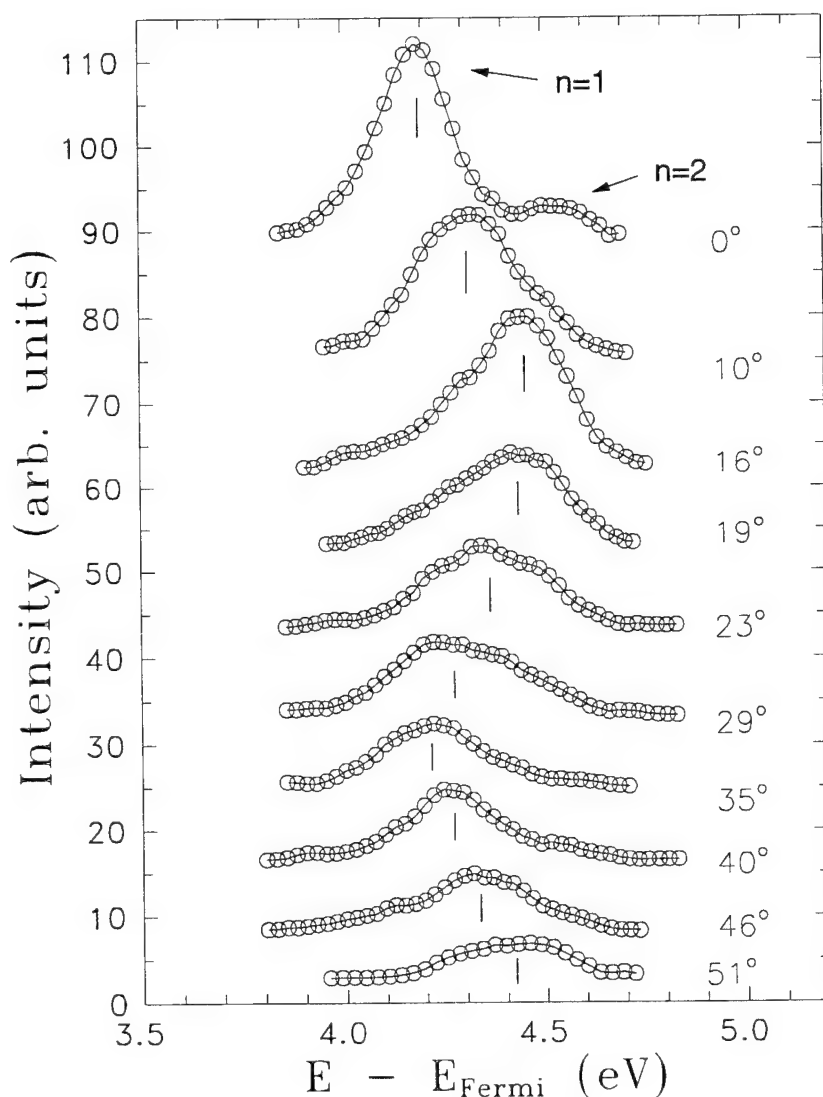

Figure 16. Similar to Fig. 15, but with a coverage of ~ 0.01 monolayer of sodium, which stabilizes an ordered step lattice. The downwards energy dispersion beyond 16° is due to back-folding by the reciprocal step lattice vector.

47

Figure 16 shows angle-resolved measurements similar to those shown in Fig. 15 for the surface dosed with ~ 0.01 ML of Na. Note that the image state was of comparable width and signal intensity to those at the bare stepped surface, a result consistent with Na atoms being located at the step edges rather than on terraces. The image-state energy was shifted *up* by ~ 0.13 eV from its value on bare stepped Cu(001), possibly due to confinement to the terrace. More importantly, the dispersive behavior of the surface is greatly improved in clarity; in fact it is clear that back-folding can be seen to occur at $\theta \geq 16°$, followed by a 'normal' dispersion trend starting at $\theta \approx 35°$. Because $k_\parallel$ is conserved during the photoemission process, one can derive the lateral wavevector of the image-state electron using $k_\parallel = (\sqrt{2m^* E_{kin}} / \hbar) \sin\theta$, where E_{kin} is the kinetic energy of the photoemitted electron above the vacuum level.
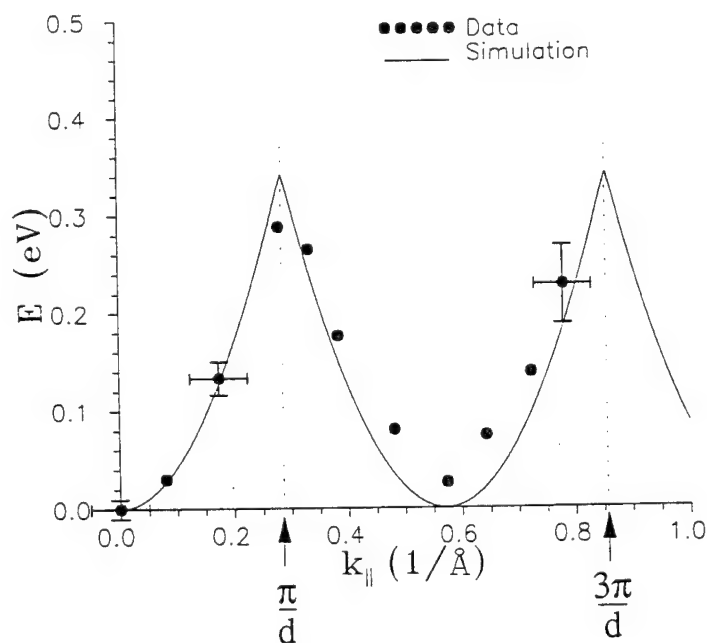

Fig. 17. The dispersion relation of the lateral superlattice formed on Na-decorated, stepped Cu(001). The filled circles are our data, the full line is a fit, and the dotted lines indicate the Brillouin zone boundaries of the step superlattice. The back-folded band between π/d and $3\pi/d$ is absent on the flat Cu(001) surface.

The plot of the transformed data E vs. $k_{\parallel}$ is shown in Fig. 17, where $E = E_{kin} - E_o$ is the electron kinetic energy above the bottom (E_o) of the image-state band. Back-folding occurs at $k_{\parallel}$ ≈ 0.29 Å^{-1}. The initial dispersion near the zone center can approximately be fitted with a free-electron-like parabolic relation with a ~15% increase in the effective mass ($m^* \approx 1.05 m_e$) for the n=1 image state, as compared to that of a planar Cu(001), where $m^* = 0.9 \, m_e$.

D. Lateral Superlattice Effects

The dispersive behavior displayed in Figs. 16 and 17 is in accord with that expected from a lateral surface superlattice, which can be provided by a stepped metal surface with a periodic modulation of the surface potential from the steps. The periodicity is given by the terrace width, d, in the dimension normal to the steps. For image-state electrons the effective magnitude of the step potential will depend on the average distance of the electron from the crystal plane. Electrons in such a 1D periodic potential will display their lateral superlattice nature with new Brillouin zones, whose size is determined by the reciprocal step-lattice vector of $g = 2\pi/d$. The electrons excited to the image state will experience Bragg reflections, which give rise to zone-folding phenomena, and can be transformed in k-space by the step lattice vector **g**, which is 4.5 times smaller than that on the flat Cu(001). The periodic step potential will result in a multivalued dispersion function which repeats itself beyond $k_{\parallel} = \pi/d$, *within* the *first* surface Brillouin zone (0 to 1.23 Å^{-1}) of the flat (001), as seen in Fig. 17. In addition, the superlattice potential would also be expected to provide additional confinement for the image-state electron, leading to a larger effective mass as mentioned above.

The differences in the dispersive behavior for the bare and the adsorbate-covered surface can be understood in terms of the behavior of steps on low-index surfaces of noble metals. In

49

particular, steps on Cu(001) are known[93] to exhibit considerable roughness at RT due to fluctuations in the thermal motion of steps on the surface, which accounts for the persistent fuzziness in the LEED pattern of the bare surface. As is apparent from our measurement of a sharper LEED pattern on the dosed surface, Na adatoms stabilize the structure, giving a more regular array of steps and thus providing a well defined lateral surface superlattice along the direction perpendicular to the steps. The solid line in Fig. 17 shows the dispersion relation of the first band obtained by evaluating a simple Kronig-Penney model[89] with a period of d = 11 Å for the step potential. Clearly, an excellent agreement between the data and simulation is achieved. The calculation shown in Fig. 17 treats the step potential as a small perturbation to the surface potential.

E. Effects of Lateral Confinement on the Binding Energy

More generally, the periodic potential would also give rise to a series of energy bands in the reduced lateral Brillouin zone; the zero-point energy and band gaps of these bands would depend on the strength and detailed structure of the step-edge potential. The Kronig-Penney model shows that simple periodic *wells* at the step sites will result in a lowering of the image-state bands while potential *barriers* lead to a upward shift in the energy band. Bipolar potentials (as sketched in Fig. 18) with equal height and width for the well and barrier at the step edge would also lead to lower energy bands. However, other combinations such as a narrower well and broader barrier or higher barrier and shallower well would yield much smaller changes in image-state binding energies. Based on recent measurements[94] of surface-electron density at step edges, a strongly asymmetric bipolar potential would be reasonable. Application of the Kronig-Penney model shows that such a bipolar potential, depending on the relative contributions of the barrier and well portion, can

50

yield relatively small changes in image-state binding energies, a situation in accord with the observation of the small binding energy shifts on stepped and planar surfaces mentioned earlier. On the Na-dosed stepped surface, the energy band of the image state appears to shift up (see Figs. 15 and 16, where the band bottom of the image state from 4.05 eV of that on the bare stepped surface to ~ 4.18 eV). Intuitively, one would expect the image state to go down in such a case because the Na adatom would cause a deeper well at the step edge and such a deeper well should result in a downward shift of the image band according to the Kronig-Penney model. However, note that an increase in barrier height on the other side of the edge at the same time, *i.e.*, a strongly asymmetric bipolar potential, would be reasonable, thus leading to a combined effect of upshifting in the image state band. Nevertheless, more information on the surface potential at the step sites is needed before our measurement of the change in binding energy can be further assessed. Incidentally, this provides a good opportunity for further collaboration between theorists and experimentalists in such a fruitful field.
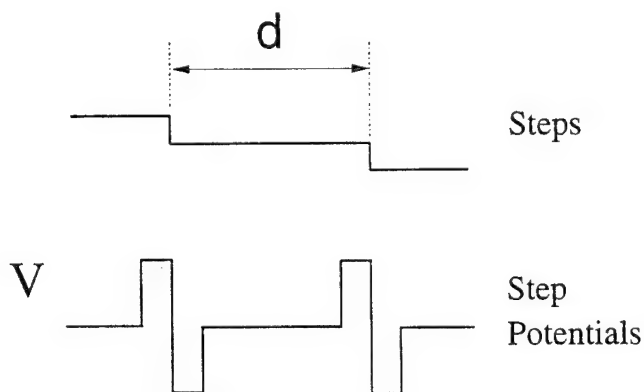

Figure 18. Diagram of bipolar potentials at a stepped surface.

F. Localization Due to Step Disorder

The fact that the dispersion on the bare stepped surface in Fig. 15 deviates from the ideal is

likely due to finite distribution in step spacings for this surface, as reflected in the fuzziness in our

LEED pattern and also noted in earlier STM studies.[93] This randomness in the step distribution

causes a distribution of back-folding vectors in our photoemission experiment. It is unimportant

near the bottom of the band, *i.e.* at the zone center and at $k_\parallel = 2\pi/d$, where the energy is

insensitive to $k_\parallel$. However, it becomes substantial at the zone boundaries, where the energy

dispersion is strong. The averaging over $k_\parallel$ due to different back-folding vectors 'washes out' the

highly-dispersive states and leaves only states at the bottom of the band. To investigate this effect

quantitatively we used the step width distribution reported for Cu(100) from STM,[93] with each

step periodicity creating its own Brillouin zone and consequently its own dispersion. Adding

contributions from all the different step periodicities at each detection angle and taking the finite

angular resolution of the detector into account, our simulation gives a set of spectra strongly

resembling Fig. 15, including the non-dispersive feature at the bottom of the band as shown in
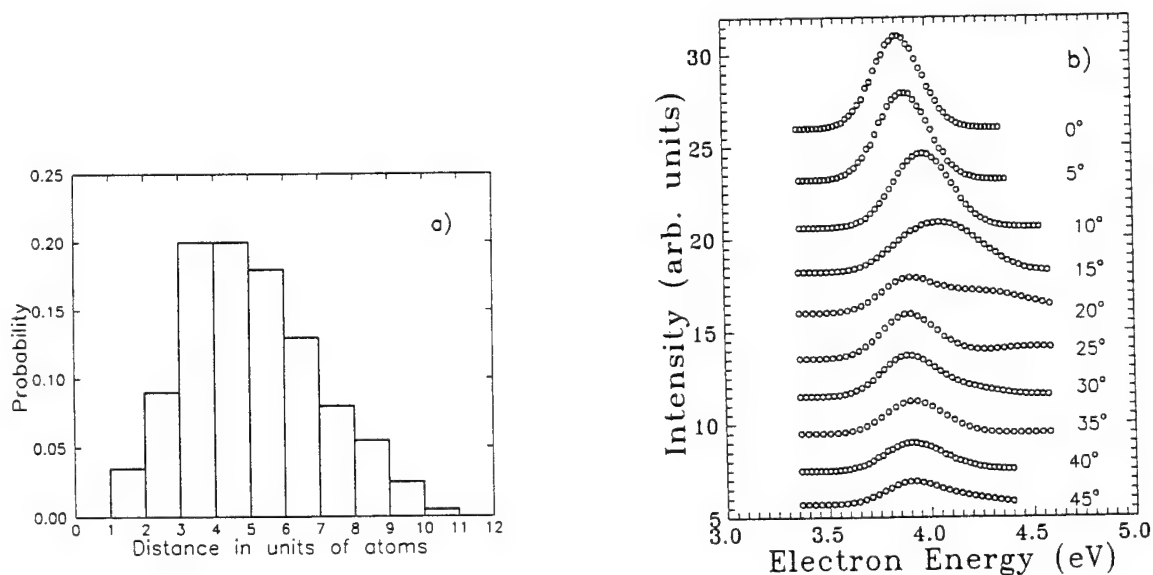
Fig. 19.

Figure 19: a) Step-width distributions on Cu(001) as obtained by STM studies; b) simulations of the averaging effects on the image-state 2PPE signals from bare vicinal Cu(001), showing step-disorder-induced localization.

If this is the case, it could be viewed as a state that is localized in the direction perpendicular to the steps by step disorder, in a manner similar to localization phenomena in amorphous semiconductors.[95]

G. Asymmetric Photoemission

Finally, the width of the photoemitted features was seen to depend on whether the detection was toward the $[\bar{1}10]$ or the $[1\bar{1}0]$ direction, i.e., whether the photoemission was 'uphill' or 'downhill' with respect to the steps. In the downhill direction the emitted features were found to be generally broader throughout the angular range, a result which was obtained for a wide range of samples and surface quality. This asymmetric behavior for electrons emitted 'uphill' vs. 'downhill' suggests asymmetric scattering at the step edge. This could be caused, for example, by asymmetric interaction with bulk bands: Emission in the uphill direction is closer to the normal of the (001) terraces than in the downhill direction. The interaction with bulk bands is weakest along the [001] direction where the bulk band gap is widest.

In summary, we have observed lateral superlattice effects on a stepped surface, where natural monatomic-height steps are formed with a periodicity of about 11 Å. On surfaces with alkali stabilization of the step edges, the angle-resolved 2PPE data clearly show a reduction of the Brillouin zone from that on the planar surface and a periodic dispersion behavior, which can be described by the classic Kronig-Penney model, throughout the first two Brillouin zones for the first band from the n=1 image state. While an exact treatment must await the application of a first-principles many-body theory, comparison with simple Kronig-Penney calculations suggests that the step-edge potential for the image-state electron is relatively weak. The results shown above clearly demonstrate that image-state spectroscopy, in conjunction with angle-resolved

53

2PPE, provides a unique and sensitive probe to the electronic structure near a surface and could

be readily applied to other low dimensional systems.

References

1. D. Straub and F. J. Himpsel, *Phys. Rev. Lett.* **52**,1922 (1984).

2. K. Giesen, F. Hage, F. J. Himpsel, H. J. Riess and W. Steinmann, *Phys. Rev. Lett.* **55**, 300 (1985).

3. W. Steinmann, *Appl. Phys.* A **49**, 365 (1989) and references given therein.

4. Z. Wu, B. Quiniou, J. Wang, and R. M. Osgood, Jr., *Phys. Rev.* B **45**, 9406 (1992).

5. B. Quiniou and R. M. Osgood, Jr., *Phys. Rev.* B **47**, 9971 (1993).

6. B. Quiniou, V. Bulovic, and R. M. Osgood, Jr., *Phys. Rev.* B **47**, 15890 (1993).

7. N. Fischer, S. Schuppler, R. Fischer, Th. Fauster, and W. Steinmann, *Phys. Rev. Lett.* **70**, 654 (1993).

8. N. Fischer, S. Schuppler, R. Fischer, Th. Fauster, and W. Steinmann, *Phys. Rev.* B **47**, 4705 (1993).

9. D.F. Padowitz, W. R. Merry, R. E. Jordan, and C.B. Harris, *Phys. Rev. Lett.* **69**, 3583 (1992).

10. X.Y. Wang, R. Paiella, and R. M. Osgood, Jr., *Phys. Rev.* B **51**, 17035 (1995).

11. X.Y. Wang, X. J. Shen, R. M. Osgood, Jr., R. Haight, and F. J. Himpsel, submitted to *Phys. Rev. Lett.*

12. F. J. Himpsel, Y. W. Mo, T. Jung, J. E. Ortega, G. J. Mankey, and R. F. Willis, *Superlattices and Microstructures* **15**, 237 (1994).

13. Y. Hasegawa and Ph. Avouris, Phys. Rev. Lett. **71**, 1071 (1993); M. F. Crommie, C. P. Lutz, and D. M. Eigler, *Nature* **363**, 524 (1993).

14. R. Haight *et al.*, Phys. Rev. Lett. **54**, 1302 (1985); R. Haight and J. Silberman, *Appl. Phys. Lett.* **57**,1548 (1990).

15. F. Finocchi, C.M. Bertoni and S. Ossicini, *Vacuum 41, 535 (1990)*.

16. M. Radny, *Surf. Sci.* **247,** 143 (1991).

17. P.M. Echenique and M.E. Uranga, *Surf. Sci., 247, 125 (1991)*.

18. A. Zangwill, *Physics at Surfaces, p. 214 (Cambridge University Press, 1988)*.

19. J.W. Gadzuk, *Surf. Sci. 43, 44 (1974)*.

20. D.M. Newns, *Phys. Rev. 178, 1123 (1969)*.

21. K. Giesen, F. Hage, F.J. Himpsel, H.J. Riess and W. Steinmann, *Phys. Rev. B 33, 5241 (1986)*.

22. G.D. Kubiak, *Surf. Sci. 201, L475 (1988)*.

23. R.W. Schoenlein, J.G. Fujimoto, G.L. Eesley and T.W. Capehart, *Phys. Rev. B 43, 4688 (1991)*.

24. W. Steinmann, *Appl. Phys. A 49, 365 (1989)*.

25. K. Giesen, F. Hage, F.J. Himpsel, H.J. Riess and W. Steinmann, *Phys. Rev. B 35, 971 (1987)*.

26. W. Eberhardt and F.J. Himpsel, *Phys. Rev. B 21, 5572 (1980)* and *Phys. Rev. B 23, 5650 (1981)*.

27. *CRC Handbook of Chemistry and Physics*, 66th edition, E-86 *(CRC Press, 1986)* and C. Kittel, *Introduction to Solid State Physics, 6th edition, p. 537 (John Wiley & Sons, 1986)*.

28. S. Schuppler, N. Fischer, Th. Fauster and W. Steinmann, *Appl. Phys. A 51, 322 (1990)*.

29. T. Wegehaupt, D. Rieger and W. Steinmann, *Phys. Rev. B 37, 10086 (1988)*

30. N.V. Smith, *Phys. Rev. B 32, 3549 (1985)*.

31. N.V. Smith and C.T. Chen, *Surf. Sci. 247, 133 (1991)*.

32. C.T. Chen and N.V. Smith, *Phys. Rev. B 35, 5407 (1987)*.

33. P.M. Echenique and J.B. Pendry, *J. Phys. C 11, 2065 (1978)*.

34. P.M. Echenique and J.B. Pendry, *Prog. in Surf. Sci. 32, 111 (1990)*.

35. P.M. Echenique, F. Flores and F. Sols, *Phys. Rev. Lett. 55, 2348 (1985)*.

36. P. de Andres, P.M. Echenique and F. Flores, *Phys. Rev. B 35, 4529 (1987)*.

37. K. Giesen, F. Hage, H. J. Riess, W. Steinmann, R. Haight, R. Beigang, R. Dreyfus, Ph. Avouris, and F. J. Himpsel, *Phys. Scr.* **35**, 578 (1987).

38. L. Jurczyszyn, *Surf. Sci. 247, 158 (1991)*.

39. M. Radny, *Surf. Sci. 231, 43 (1990)*.

40. S.A. Lindgren and L. Wallden, *Phys. Rev. B 40, 11546 (1989)*.

41. S. Papadia, M. Persson and L.-A. Salmi, *Phys. Rev. B 41, 10237 (1990)*.

42. L. Jurczyszyn, *Surf. Sci. 259, 65 (1991)*.

43. D. Heskett, K. -H. Frank, and E. E. Koch, *Phys. Rev.* **B 36**, 1276 (1987).

44. D. P. Woodruff, W. A. Royer, and N. V. Smith, *Phys. Rev.* **B 34**, 764 (1986).

45. A. Goldmann, *Surf. Sci.* **178**, 210 (1986).

46. For our estimate, we have taken the experimental resolution into account, and also assumed that the inverse photoemission spectrum reflects the surface density of states.

47. W. Jacob, V. Dose, U. Kolac, Th. Fauster and A. Goldmann, *Z. Phys. B 63, 459 (1986)*.

48. E. Dietz and F.J. Himpsel, *Solid State Comm.* **30**, 235 (1979).

49. J. K. Grepstad, P. O. Gartland, and B. J. Slagsvold, *Surf. Sci.* **57**, 348 (1976).

50. P. O. Gartland, *Surf. Sci.* **62**, 183 (1977).

51. H. B. Nielsen, G. Brostroem, and E. Matthias, *Z. Phys. B* **77**, 91 (1989).

52. N. Fischer *et al.*, *Phys. Rev. B* **42**, 9717 (1990).

53. S. Schuppler, N. Fischer, Th. Fauster, and W. Steinmann, *Phys. Rev. B* 46, 13539 (1992).

54. W. R. Merry, R. E. Jordan, D. F. Padowitz, and C. B. Harris, *Surf. Sci.* **295**, 393 (1993).

55. R. W. Schoenlein *et al.*, *Phys. Rev. Lett.* **61**, 2596; *Phys. Rev. B* **41**, 5436 (1990).

56. Th. Fauster and W. Steinmann, in *Electromagnetic Waves: Recent Developments in Research, Vol. 2: Photonic Probes of Surfaces*, edited by P. Halevi (Elsevier, Amsterdam, 1995).

57. T. S. Rahman and D. L. Mills, *Phys. Rev. B* **21**, 1432 (1980).

58. S. D. Kevan, *Phys. Rev. Lett.* **50**, 526 (1983); J. Tersoff and S. D. Kevan, *Phys. Rev. B* **28**, 4267 (1983).

59. J. J. Quinn, *Phys. Rev.* **126**, 1453 (1962).

60. W. H. Knox, D.S. Chemla, G. Livescu, J.E. Cunningham, and J.E. Henry, *Phys. Rev. Lett.* **61**, 1290 (1988); R. H. M. Groenveld, Rudolf Sprik, and A. Lagendijk., *Phys. Rev. B* **45**, 5079 (1992); X. Y. Wang, D. M. Riffe, Y. -S. Lee, and M. D. Downer, *Phys. Rev. B* **50**, 8016 (1994).

61. E. G. McRae, *Rev. Mod. Phys.* **51**, 541 (1979); F. J. Himpsel, *Adv. Phys.* **32**, 1 (1983).

62. E. H. Rhoderick and R. H. Williams, *Metal-Semiconductor Contacts* (Oxford Science Publications, Oxford, 1988); J. Singh, *Physics of Semiconductors and Their Heterostructures* (McGraw-Hill, New York, 1993).

63. H. P. Bonzel, A. M. Bradshaw, and G. Ertl, *Physics and Chemistry of Alkali Metal Adsorption* (Elsevier, Amsterdam, 1989); Prog. Surf. Sci. **42** (1993).

64. W. Steinmann, *Appl. Phys.* **A49**, 365 (1989).

65. N. Fischer, S. Schuppler, R. Fischer, Th. Fauster, and W. Steinmann, *Phys. Rev. B* **47**, 4705 (1993).

66. T. Ando, A. B. Fowler, and F. Stern, *Rev. Mod. Phys.* **54**, 437 (1982).

67. F. Stern and W. E. Howard, *Phys. Rev.* **163**, 816 (1967).

68. P. O. Gartland and B. J. Slagsvold, *Phys. Rev. B* **12**, 4047 (1975).

69. Y. Jee, M. F. Becker, and R. M. Walser, *J. Opt. Soc. Am. B* **5**, 648 (1988).

70. X. Shi, D. Tang, D. Heskett, K. D. Tsuei, H. Ishida, and Y. Morikawa, *Surf. Sci.* **290**, 69 (1993).

71. R. Fischer, S. Schuppler, N. Fischer, Th. Fauster and W. Steinmann, *Phys. Rev. Lett.* **70**, 654 (1993).

72. S. D. Kevan, *Phys. Rev. B* **33**, 4364 (1986); S. D. Kevan, *Surf. Sci.* **178**, 229 (1986).

73. N. V. Smith, P. Thiry, and P. Petroff, *Phys. Rev. B* **47**, 15476 (1993).

74. J. A. Knapp, F. J. Himpsel, and D. E. Eastman, *Phys. Rev. B* **19**, 4952 (1979).

75. C.A. Schmuttenmaer, M. Aeschlimann, H.E. Elsayed-Ali, D.A. Mantell, J. Cao, Y. Gao, and R.J.D. Miller, *Phys. Rev. B* **50**, 8957 (1994).

76. See, for example, L. I. Schiff, *Quantum Mechanics* (McGraw-Hill, New York, 1968).

77. L. J. Clarke, *Surface Crystallography* (John Wiley & Sons, New York, 1985).

78. D. Straub and F. J. Himpsel, *Phys. Rev.* **B** 33, 2256 (1986).

79. T. Ando, A. B. Fowler, and F. Stern, *Rev. Mod. Phys.* **54**, 437 (1982).

80. C. Gourgon *et al.*, *J. Crystal Growth* **138**, 590 (1994).

81. J. E. Ortega and F. J. Himpsel, *Phys. Rev. Lett.* **69**, 844 (1992).

82. S. S. P. Parkin, *Phys. Rev. Lett.* **67**, 3598 (1991).

83. D. E. Heim *et al.*, *IEEE Trans. Mag.* **30**, 316 (1994).

84. J. E. Ortega and F. J. Himpsel, *Appl. Phys. Lett.* **64**, 121 (1994).

85. J. E. Ortega, F. J. Himpsel, R. Haight, and D. R. Peale, *Phys. Rev.* **B 49**, 13859 (1994).

86. R. S. Williams *et al.*, *Phys. Rev. Lett.* **41**, 323 (1978); A. P. Shapiro *et al.*, *Phys. Rev.* **B 38**, 1779 (1988).

87. O. Sanchez, J. M. Garcia, P. Segovia, J. Alvarez, A. I. Vazquez de Parga, J. E. Ortega, M. Prietsch, R. Miranda, to be published.

88. H. Wagner, in *Springer Tracts in Modern Physics*, Vol. 85 (ed. by J. Holzl, F. K. Schulte, and H. Wagner, 1979), p. 151–221.

89. H. M. Rosenberg, *The Solid State* (Oxford, 1988).

90. R. Schneider, H. Durr, Th. Fauster, and V. Dose, *Phys. Rev.* **B 42**, 1638 (1990).

91. E. V. Albano and H. O. Martin, *Phys. Rev.* **B 38**, 7932 (1988); S. Kennou *et al.*, *Surf. Sci.* **216**, 462 (1989).

92. T. Aruga *et al.*, *Phys. Rev. B* **34**, 8237 (1986); N. C. Bartelt *et al.*, *Surf. Sci.* **240**, L591 (1990); C. Jayaprakash *et al.*, *Phys. Rev. B* **30**, 6549 (1984).

93. J. Frohn *et al.*, Phys. Rev. Lett., **67**, 3543(1991); M. Poensgen *et al.*, *Surf. Sci.*, **274**, 430 (1992).

94. Ph. Avouris, I. -W. Lyo, and P. Molinas-Mata, to be published.

95. P.W. Anderson, *Phys. Rev.* **109**, 1492 (1958).

Appendix A: Presentations and Publications Under the Present ARO Project

1. R.M. Osgood, Jr., "Manipulating Electrons at Surfaces with Light," American Physical Society, Laser Science Topical Group: Traveling Lecturer Program, University of Colorado, Boulder, Colorado, January 12, 1993.

2. R.M. Osgood, Jr., "Light-Control of Semiconductor Surface Chemistry," University of Pennsylvania, Frontiers in Materials Science Lecture, Philadelphia, PA, January 15, 1993.

3. R.M. Osgood, Jr., "Time of Flight Studies of Electron-Transfer-Induced Reactions on GaAs(110)," 20th Conference on the Physics and Chemistry of Semiconductor Interfaces PCSI '93, American Vacuum Society, Colonial Williamsburg, PA, January 25-29, 1993.

4. R.M. Osgood, Jr., Q.Y. Yang, W.N. Schwarz, S. Hood, N. Loo, P. Lasky, "Laser Manipulation of Surface Electrons," American Physical Society, Laser Science Topical Group: Traveling Lecturer Program, Franklin and Marshall College, Lancaster, PA, February 18, 1993.

5. R.M. Osgood, Jr., "Photochemistry on Semiconductor Surfaces," Spring 1993 STC Seminar, University of Texas at Austin, Austin, TX, February 22, 1993.

6. B. Quiniou and R.M. Osgood, Jr., "Image-Potential States and Surface Plasmons: temperature dependence," Phys. Rev. B **47**, 9971 (1993).

7. Vladimir Bulovic, B. Quiniou and R.M. Osgood, Jr., "Observation of Image-Potential-Induced Resonances on Cu(110)," QELS '93, Optical Society of America, Baltimore, MD, May 3, 1993.

8. R.M. Osgood, Jr., "Laser Manipulation of Surfaces," Bard College, Annandale-on-Hudson, NY, May 11, 1993.

9. R.M. Osgood, Jr., "Monolayer Surface Chemistry for Processing of III-V Semiconductors," American Chemical Society Meeting, MARM '93, Hofstra University, Hempstead, Long Island, New York, June 4, 1993.

10. V. Bulovic, B. Quiniou, and R.M. Osgood, Jr., "Image-Potential-Induced Resonance on Al(111) Observed by Two-Photon Photoemission Spectroscopy," submitted to AVS 1993, Orlando, Florida, November 15-19, 1993.

11. V. Bulovic, B. Quiniou and R.M. Osgood, Jr., "Observation of Image-Potential-Induced Resonances on Cu(110) Using the Two-Photon Photoemission Technique," Phys. Rev. B. <u>47</u>, 15 890 (1993).

12. R. Paiella, X.Y. Wang, and R.M. Osgood, Jr. "Overlayer Coverage Dependence of Surface States for Cs on Cu(100)," presented at the American Physical Society Meeting, March 21-25,

1994, Pittsburgh, PA.

13. R.M. Osgood, Jr. "Manipulation of Electrons at Surfaces." Invited talk at Polytechnic University, Condensed Matter Seminar, February 2, 1994, Brooklyn, NY.

14. R.M. Osgood, Jr. (B. Quiniou, V. Bulovic, Z. Wu, X. Wang) "Nonlinear photoemission of image states: a new 'high-resolution' surface spectroscopy." Invited talk at OE/LASE '94: Laser Techniques for Surface Science, January 27-29, 1994, Los Angeles, CA.

15. X.Y. Wang, R. Paiella, and R.M. Osgood, Jr. "Alkali-Coverage Dependence of Image-State Quenching on Single-Crystal Cu Surfaces." Presented at the American Physical Society 54th Annual Conference on Physical Electronics, June 13-15, 1994, Knoxville, TN.

16. V. Bulovic, B. Quiniou, and R.M. Osgood, Jr., "Image-Potential-Induced Resonances on Al(111) Observed by Two-Photon Photoemission," J. Vac. Sci. Technol. A, 12, 2201 (1994).

17. R.M. Osgood, Jr., "Image States on Single Crystal Metals: High Resolution Spectroscopy for Condensed Matter," Harvard Physics Colloquium, December 2, 1994.

18. R.M. Osgood, Jr., "Image States on Single Crystal Metals: Rydberg Spectroscopy for Condensed Matter," MIT Atomic Physics Seminar, December 9, 1994.

19. X.Y. Wang, R. Paiella, and R.M. Osgood, Jr., "Two-Dimensional Electron Scattering Processes on Na-Dosed Cu(111): A Two-Photon Photoemission Study," Phys. Rev. B 51, 17 035(1995).

20. X.Y. Wang, X.J. Shen, and R.M. Osgood, Jr., "Reduced-Dimensional Electron Confinement on Stepped Cu(100)," 55th Physical Electronics Conference, Flagstaff, AZ, June 12-14, 1995.

21. X.Y. Wang, R. Paiella, and R.M. Osgood, Jr, "Two-photon-photoemission Study of 2D Scattering on Na-Covered Cu Surfaces," 1995 CLEO/QELS, Baltimore, MD, May 24, 1995.

22. X.Y. Wang, X.J. Shen, R. Haight, F.J. Himpsel, and R.M. Osgood, Jr., "Observation of Lateral Superlattice Effects on Stepped Cu(001)," submitted to Phys. Rev. Lett. (July 1995).

Appendix B: Scientific Personnel Who Participated in the Present ARO Project

Mr. Vladimir Bulovic, Awarded the M.S. in Electrical Engineering

Mr. Konstantin Melnikov, Graduate Student

Mr. Roberto Paiella, Awarded the M.S. in Electrical Engineering

Dr. Bertrand Quiniou, Awarded the Ph.D. in Applied Physics.

Dr. Xiaoyi Wang, Postdoctoral Research Scientist

Mr. Yubo Wang, Undergraduate Student